Carbon dioxide dissolution in structural and stratigraphic traps

Carbon dioxide dissolution in structural and stratigraphic traps

M. L. SZULCZEWSKI[1], M. A. HESSE[2], AND R. JUANES[1]

[1]Department of Civil and Environmental Engineering, Massachusetts Institute of Technology, Cambridge, MA, USA

[2]Department of Geological Sciences and Institute for Computational Engineering and Sciences, University of Texas at Austin, Austin, TX, USA

(Received ?? and in revised form ??)

The geologic sequestration of carbon dioxide (CO_2) in structural and stratigraphic traps is a viable option to reduce anthropogenic emissions. While dissolution of the CO_2 stored in these traps reduces the long-term leakage risk, the dissolution process remains poorly understood in systems that reflect the appropriate subsurface geometry. Here, we study dissolution in a porous layer that exhibits a feature relevant for CO_2 storage in structural and stratigraphic traps: a finite CO_2 source along the top boundary that extends only part way into the layer. This feature represents the finite extent of the interface between free-phase CO_2 pooled in a trap and the underlying brine. Using theory and simulations, we describe the dissolution mechanisms in this system for a wide range of times and Rayleigh numbers, and classify the behavior into seven regimes. For each regime, we quantify the dissolution flux numerically and model it analytically, with the goal of providing simple expressions to estimate the dissolution rate in real systems. We find that, at late times, the dissolution flux decreases relative to early times as the flow of unsaturated water to the CO_2 source becomes constrained by a lateral exchange flow though the reservoir. Application of the models to several representative reservoirs indicates that dissolution is strongly affected by the reservoir properties; however, we find that reservoirs with high permeabilities ($k \geqslant 1$ Darcy) that are tens of meters thick and several kilometers wide could potentially dissolve hundreds of megatons of CO_2 in tens of years.

1. Introduction

Geologic sequestration of carbon dioxide is a promising option to mitigate climate change (Lackner 2003; IPCC 2005; Schrag 2007; Benson & Cole 2008; Orr 2009). The first stage of the process is capturing anthropogenic CO_2 from large, stationary sources such as power plants and transporting it to a storage site. At the storage site, the next stage is injecting the CO_2 underground for long-term storage into regions of deep, porous rock such as structural and stratigraphic traps.

Structural and stratigraphic traps are regions of porous rock in which an overlying, low-permeability seal exhibits a concave-down geometry (IPCC 2005). In structural traps, this geometry is due to either a large-scale fold in the reservoir or the intersection of a sealing fault with a dipping region of the reservoir. In the case of a fold, the seal is typically a layer of fine-grained rock such as shale or mudstone called a caprock; in the case of a fault, the seal is due to both the caprock and impermeable material within the fault. In stratigraphic traps, the concave-down shape is due to changes in rock type. For example, a dipping reservoir may pinch out between two layers of fine-grained rock or terminate in a unconformity against fine-grained rock (figure 1).

Structural and stratigraphic traps are attractive sites for CO_2 sequestration (Gunter *et al.* 2004). Their low-permeability seal inhibits the upward migration of CO_2, reducing the risk of leakage to a shallower formation or the surface. While a low-permeability seal can be present at many locations in a reservoir, structural and stratigraphic traps are particularly appealing because their concave-down geometry also constrains the lateral spread of CO_2, reducing the risk that it will migrate away from the injection site to potential leakage pathways such as *non-sealing* faults or abandoned wells. Another attractive feature is that many traps have proven seals. When the trap is located in an oil and gas field, for example, the seal quality is confirmed by the fact that it has retained buoyant hydrocarbons for millions of years.

While structural and stratigraphic traps reduce the risk of CO_2 leakage, they do not eliminate it. The seal may contain small fractures or faults that allow leakage but that are not identified in the characterization stage of a sequestration project. In the injection stage, the seal may be compromised by accidentally overpressurizing the reservoir, which could hydraulically fracture the seal or cause slip along a pre-existing fault in the seal (Grasso 1992; Rutqvist & Tsang 2002; Chiaramonte *et al.* 2008; Mathias *et al.* 2009). After the injection well has been closed, the seal may be damaged by seismic activity or human activity in the subsurface close to the reservoir.

Dissolution of the CO_2 into the groundwater mitigates the risk of leakage from an imperfect or compromised seal. This is because water with dissolved CO_2 is more dense than the ambient groundwater, and will tend to sink rather than rise though a leakage pathway. Estimating the dissolution rate will help constrain the quantity of CO_2 that will remain in the target reservoir, and the quantity that will escape.

CO_2 dissolution has been well studied in idealized systems. These systems commonly include laterally infinite porous layers (Ennis-King *et al.* 2005; Xu *et al.* 2006; Riaz *et al.* 2006; Slim & Ramakrishnan 2010), laterally periodic porous layers (Rapaka *et al.* 2008; Pau *et al.* 2010; Hidalgo *et al.* 2012), and laterally closed porous layers in which the side walls are no-flow boundaries (Riaz *et al.* 2006; Hassanzadeh *et al.* 2007; Neufeld *et al.* 2010; Kneafsey & Pruess 2010; Backhaus *et al.* 2011; Hewitt *et al.* 2013; Slim *et al.* 2013). The systems typically include only the porous layer below the CO_2-brine interface, and represent the interface via a top boundary fixed at CO_2 saturation. In these systems, dissolution initially occurs via diffusion only, leading to a diffuse boundary layer of CO_2-rich fluid below the top boundary. Since the boundary layer is more dense than the underlying fluid, it is unstable and breaks up into descending fingers after a time proportional to D/V^2, where D is the effective diffusion coefficient and V is the characteristic buoyancy velocity, as defined in §2 (Ennis-King *et al.* 2005; Xu *et al.* 2006; Riaz *et al.* 2006; Hassanzadeh *et al.* 2007; Slim & Ramakrishnan 2010). Due to conservation of mass, underlying fluid at lower CO_2 concentrations simultaneously rises upward, leading to sharp concentration gradients at the top boundary that increase the dissolution flux. The exact expression of the enhanced dissolution flux remains controversial: some studies suggest it depends on the Rayleigh number (Backhaus *et al.* 2011; Neufeld *et al.* 2010), while others indicate it is independent (Pau *et al.* 2010; Hidalgo *et al.* 2012). After the fingers reach the bottom of the reservoir, dissolved CO_2 begins to circulate back to the top, lowering the concentration gradients and causing the dissolution rate to continually decrease (Slim *et al.* 2013; Hewitt *et al.* 2013).

Here, we study CO_2 dissolution in a porous layer that more closely reflects storage in a structural or stratigraphic trap. Like most previous studies, we represent the interface between the free-phase CO_2 and groundwater via a boundary condition: we fix the concentration along the top boundary at the saturated CO_2 concentration. Unlike many studies, however, we apply this condition along only part of the top boundary to repre-

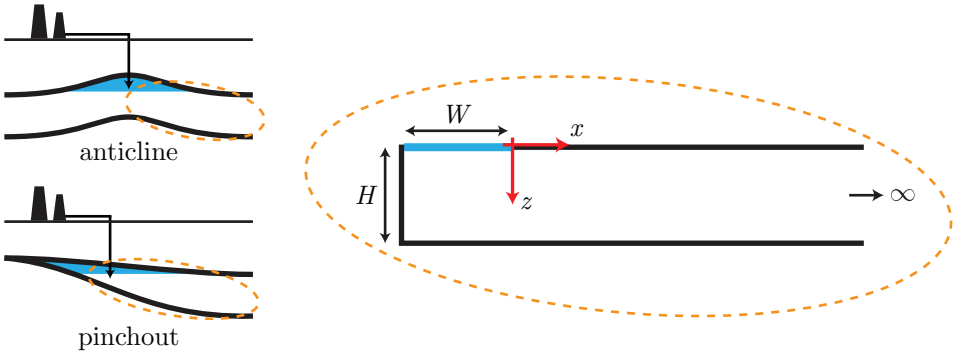

FIGURE 1. We study CO_2 dissolution in a porous layer that exhibits features of structural traps such as anticlines and stratigraphic traps such as pinchouts between low-permeability rock. The layer is semi-infinite to represent the large lateral extent of a deep, geologic reservoir. A portion of the top boundary (blue line) is held at the saturated CO_2 concentration to represent the finite CO_2-groundwater interface.

sent the finite extent of the interface. To account for the observation that many traps exist in reservoirs that are laterally extensive relative to the thickness of the layer and width of the trap, we set the right boundary at infinity. This combination of a finite CO_2 source in a laterally extensive layer represents either a stratigraphic trap or a structural trap like an anticline that is nearly symmetric about its axial plane (figure 1).

While this system represents a geologic trap, it is an idealization. In contrast to an actual trap, the porous layer is two dimensional, homogeneous, isotropic, rectilinear, and perfectly horizontal. There is also no natural background flow and we neglect hydrodynamic dispersion. We invoke these simplifications to focus on the physics of dissolution from a finite CO_2 source, and address some of the limitations they entail in the Application section.

In contexts outside of CO_2 sequestration, some studies have investigated natural convection in geometries similar to our idealized CO_2 trap. Elder (1967) studied heat transfer in a porous medium in which a portion of the lower boundary was held at an elevated temperature. This system, sometimes called the Elder problem, is similar to ours in that both involve a laterally finite source modeled by a Dirichlet boundary condition; it differs in that the medium is finite and the remaining walls are all held at zero temperature, so a steady-state exists. Wooding *et al.* (1997*a*) and Wooding *et al.* (1997*b*) studied the infiltration of dense, saltwater fingers into a porous layer from an overlying salt lake. This system, often called the salt-lake problem, is also similar to ours in that it involves a finite source; it differs in that the lake exhibits evaporative loss, which both concentrates the salt and drives convection from the surrounding area to the lake, partially stabilizing the saline boundary layer. Cheng & Chang (1976) studied boundary-layer flow in a porous medium partially overlain by a cold boundary or partially underlain by a hot boundary. This system is similar to ours in the same way as the Elder and salt-lake problems. However, it differs in that the domain is laterally infinite and vertically semi-infinite. Furthermore, due to the boundary-layer approximation, the analysis of Cheng & Chang (1976) can not capture fingering or any subsequent behavior. While all of these studies provide insight into natural convection from a finite source, they provide a limited understanding of how CO_2 dissolves in the subsurface.

We find that CO_2 dissolution in our idealized geologic trap occurs through several mechanisms. These mechanisms vary spatially along the length of the CO_2 source: along

the inner regions of the source far from the edge, the dissolution mechanisms are nearly identical to those observed in previous studies of convective CO_2 dissolution; near the edge, however, the mechanisms are novel and are strongly impacted by flow in the porous layer outside the source region. The dissolution mechanisms also vary temporally, and the different periods of behavior can be organized into seven regimes (figure 2). For each regime, we describe the mechanisms and quantify the dissolution flux numerically. We also develop an analytical model of the dissolution flux in each regime, with the goal of providing simple expressions to estimate dissolution rates that can be expected in practice.

2. Governing equations

Under the Boussineq approximation, the density-driven flow of incompressible, miscible fluids in a porous medium is described by the following system of equations (Nield & Bejan 2013):

$$\boldsymbol{\nabla} \cdot \boldsymbol{u} = 0, \tag{2.1}$$

$$\boldsymbol{u} = -\frac{k}{\mu\phi}\left(\boldsymbol{\nabla} p - \rho(c) g \hat{\boldsymbol{z}}\right), \tag{2.2}$$

$$\frac{\partial c}{\partial t} + \boldsymbol{u} \cdot \boldsymbol{\nabla} c - D\nabla^2 c = 0. \tag{2.3}$$

Equation 2.1 expresses conservation of mass for the entire fluid mixture, equation 2.2 is Darcy's law, and equation 2.3 is the concentration equation. We solve these equations in two dimensions. The variables are as follows: c is the CO_2 concentration, D is the effective diffusion coefficient, k is the permeability, μ is the dynamic viscosity, ϕ is the porosity, p is the pressure, g is the gravitational acceleration, ρ is the density, and $\boldsymbol{u} = (u, v)$ is the pore velocity (sometimes called the intrinsic, volume-averaged velocity). We take the effective diffusion coefficient, D, the permeability, k, the dynamic viscosity, μ, and the porosity, ϕ, as constants. We assume the density, ρ, is a linear function of the concentration: $\rho = \rho_0 + \Delta\rho \frac{c}{c_s}$, where ρ_0 is the density of freshwater, $\Delta\rho$ is the density difference between freshwater and CO_2-saturated water, and c_s is the saturated concentration of CO_2. Substituting Darcy's law into equation 2.1 yields the pressure equation:

$$\nabla^2 p = g\frac{\partial \rho}{\partial z}. \tag{2.4}$$

Taking the curl of Darcy's law yields the vorticity equation:

$$\omega = \frac{\partial u}{\partial z} - \frac{\partial v}{\partial z} = -V\frac{\partial c'}{\partial x}, \tag{2.5}$$

where ω is the vorticity in the direction normal to the system (see figure 1), c' is the concentration normalized to the saturated concentration ($c' = c/c_s$), and $V = \Delta\rho g k/\mu\phi$ is the characteristic buoyancy velocity. This equation shows that lateral concentration gradients drive vortical flow.

The initial condition is that the velocity and concentration are zero everywhere:

$$\boldsymbol{u}(x, z, t = 0) = \boldsymbol{0}, \qquad c(x, z, t = 0) = 0. \tag{2.6}$$

The boundary condition for the concentration equation along the top of the layer is

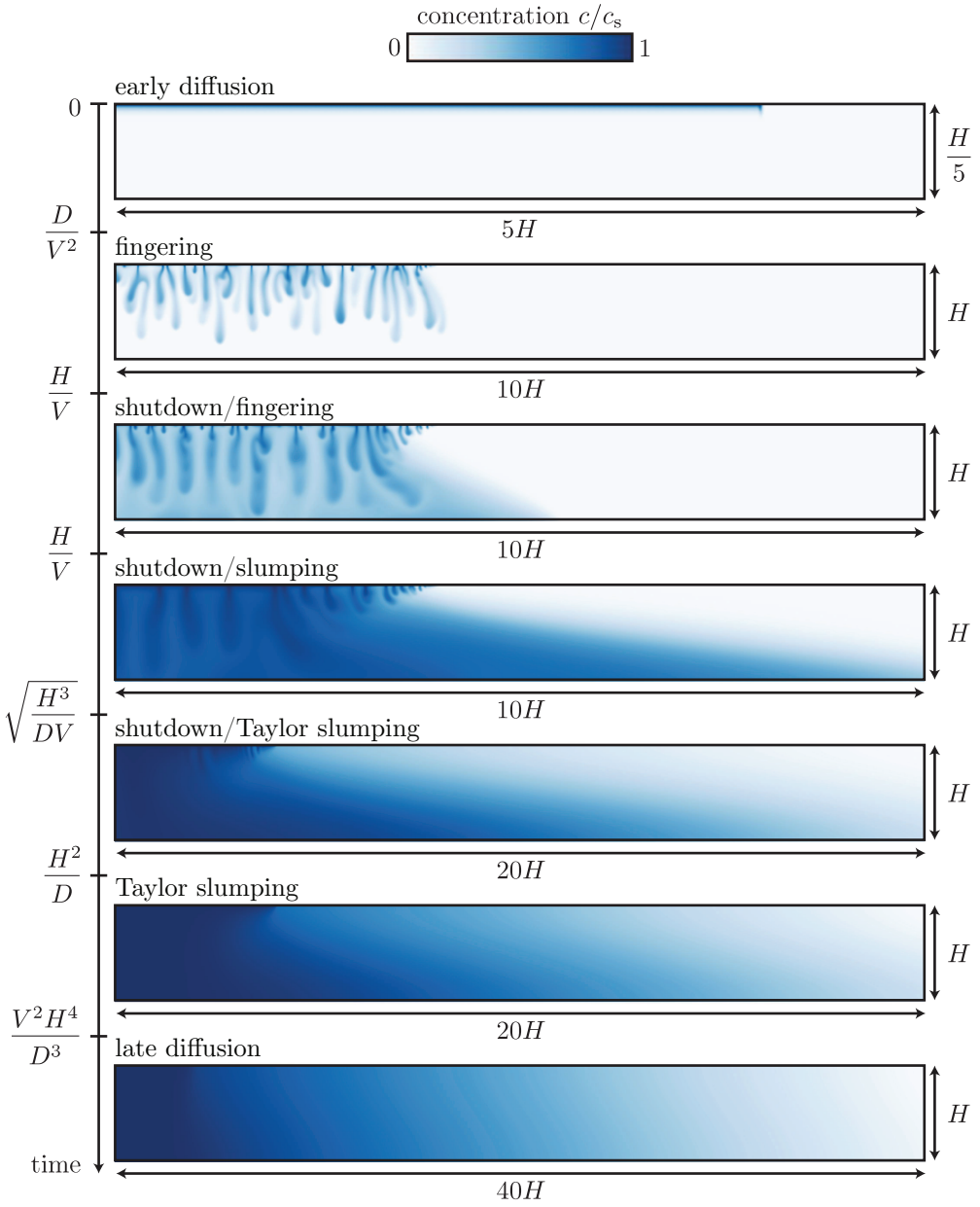

FIGURE 2. Dissolution evolves through the seven regimes shown here ($Ra = 3000$). The color scale represents the concentration of CO_2, c, normalized to the saturated concentration, c_s. The scalings of the transition times between the regimes are shown in terms of the layer thickness, H, the effective diffusion coefficient, D, and the characteristic velocity, $V = \Delta\rho g k/\mu\phi$ (see §2). When $Ra = VH/D$ is sufficiently small, the first and final transition times become equal, the duration of the intermediate regimes becomes zero, and the system transitions directly to the late diffusion regime.

defined piecewise:

$$c(z=0, -W \leqslant x \leqslant 0) = c_\mathrm{s}, \qquad \left.\frac{\partial c}{\partial z}\right|_{z=0,x>0} = 0, \tag{2.7}$$

where W is the width of the CO_2 source (figure 1). For most of the study, we perturb the constant-concentration boundary condition with random noise such that the mean concentration at the boundary remains at the saturated concentration:

$$c(z=0, -W \leqslant x \leqslant 0) = c_\mathrm{s}[1 - \varepsilon + 2\varepsilon r(x)], \tag{2.8}$$

where $\varepsilon = 1 \times 10^{-3}$ is the maximum magnitude of the noise and $r(x)$ is a random number between 0 and 1. However, in analyzing the first regime, early diffusion, we initially consider a boundary condition that is unperturbed beyond numerical error. The remaining boundary conditions are no-diffusion on the bottom and left walls and no-flow on all walls; the right wall is infinitely far away:

$$v(z=0, H) = u(x=-W, \infty) = \left.\frac{\partial c}{\partial z}\right|_{z=H} = \left.\frac{\partial c}{\partial x}\right|_{x=-W,\infty} = 0. \tag{2.9}$$

The key variable we use to characterize the system is the mean dissolution flux. The point flux, f, is defined at every location along the CO_2-brine interface via Fick's law; the mean dissolution flux through the interface, $\overline{f}$, is the lateral average:

$$f(x,t) = -D\left.\frac{\partial c}{\partial z}\right|_{z=0}, \qquad \overline{f}(t) = \frac{1}{W}\int_{-W}^{0} f(x,t)\,dx. \tag{2.10}$$

When all the equations are made dimensionless, there are two governing parameters. One is the Rayleigh number, $Ra = VH/D$, which compares the strength of advection to diffusion. The second is the dimensionless width of the CO_2 source. For regimes after the fingers reach the bottom of the layer, we typically use the layer thickness, H, to non-dimensionalize the width. Since we expect the length of the CO_2-brine interface to be larger than the reservoir thickness in practice, we focus on systems for which $W \geqslant 4H$. For earlier regimes, we find that the dissolution behavior is not affected by the layer thickness, and instead use the only remaining length scale to non-dimensionalize the width: the most unstable wavelength, λ_c, which roughly reflects the characteristic finger width immediately after the onset of fingering. Based on the results of stability analyses, we define the most unstable wavelength to be $\lambda_\mathrm{c} = 90D/V$ (Ennis-King *et al.* 2005; Xu *et al.* 2006; Riaz *et al.* 2006), which agrees with our numerical results.

In general, we solve the governing equations numerically. We integrate the pressure equation using finite volumes and solve it with a fast Poisson solver (Strang 2007). To solve the concentration equation (eq 2.3), we also integrate using finite volumes, but additionally employ linear reconstructions and the MC limiter to maintain second-order accuracy (LeVeque 2002). We integrate in time using Runge-Kutta methods (Lambert 1991): for short-time simulations, we use an explicit, two-stage method, and for longer simulations, we switch to an implicit-explicit two-stage method to remove the time-step restriction from the diffusion term (Ascher *et al.* 1997). Both time integration methods are second-order accurate. We have performed a convergence analysis to confirm that the numerical method and discretizations used are sufficient to quantify the dissolution flux accurately.

3. Dissolution regimes

Early diffusion (ed). At the earliest times, dissolution occurs via diffusion without

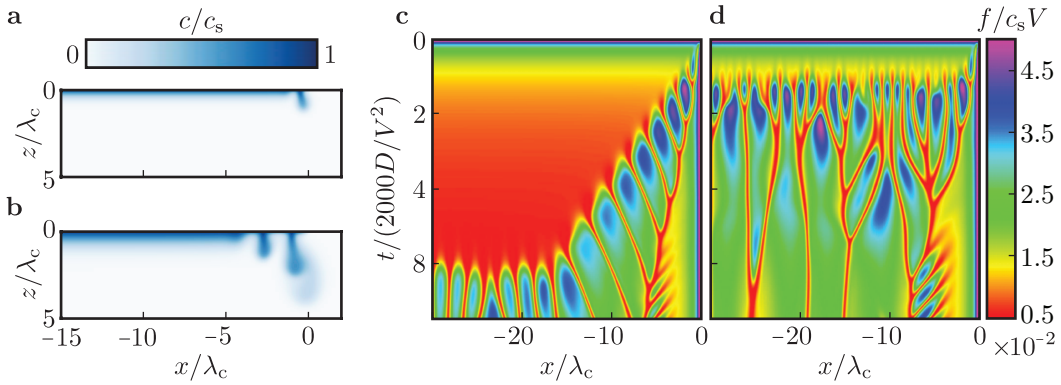

FIGURE 3. Initially, dissolution occurs via diffusion without convection along the interior of the CO_2 source, but convection occurs immediately at the edge (all results for $Ra = 4000$). **a.** Convection causes a single finger to form at the edge for high Ra ($t = 927D/V^2$, $\lambda_c = 90D/V$), as shown by this zoomed-in image of the top boundary (the bottom boundary is at $z/\lambda_c \approx 44$). **b.** This finger triggers the formation of an adjacent finger ($t = 3015D/V^2$). **c.** The evolution of fingering for longer times can be shown in a surface plot of the point fluxes along the source as a function of time. Since finger roots are highly saturated, the vertical concentration gradient immediately above a finger is small, and the dissolution flux is therefore also small. As a result, the dark red branches in the plot trace the finger movements. The plot shows that fingering propagates inward until the entire source becomes unstable. Here, a small perturbation is present ($\varepsilon = 1 \times 10^{-14}$), so the fingering front can advance far to the left before the perturbation triggers fingering everywhere. **d.** When a larger perturbation is present ($\varepsilon = 1 \times 10^{-3}$), the perturbation triggers fingering across the whole source relatively quickly before the fingering front can advance far from the edge.

convective enhancement in regions far from the edge of the source. This process creates a diffuse layer of CO_2-rich fluid directly under the top boundary.

At the edge of the source, however, convection begins immediately since the smallest amount of diffusion leads to a lateral concentration gradient there, which drives vortical flow (eq. 2.5). For $Ra \gtrsim 55$, this flow creates a single finger at the edge (figure 3**a**), as has been observed in the Elder and salt-lake problems (Elder 1967; Wooding *et al.* 1997*a*,*b*). The propagation of this finger perturbs a neighbouring region of the diffuse, CO_2-rich boundary layer, which locally destabilizes the layer and creates an adjacent finger (figure 3**b**). This process successively triggers fingering along the source until other perturbations—either numerical or physical—destabilize the entire boundary layer (figure 3**c**). For the remainder of the study, we impose random perturbations in the constant-concentration boundary of magnitude $\varepsilon = 1 \times 10^{-3}$ as shown in equation 2.8. Under this perturbation, only one or two fingers form at the edge before the entire boundary layer destabilizes (figure 3**d**). This choice is motivated by the expectation that large perturbations will be present during CO_2 storage in real geologic traps.

When the length of the CO_2 source is large, the initial convection exerts a negligible effect on the mean dissolution flux. For the perturbation we impose and $Ra \lesssim 55$, the initial convection is negligible provided $W \gtrsim 4H$. For $Ra \gtrsim 55$, fingering occurs at the edge, so the domain must be much larger than the characteristic width of a finger for the fingering process to be negligible. Numerically, we find that convection is negligible provided $W \gtrsim 30\lambda_c$. When convection is negligible, the flux may be modeled by the flux for a 1D-diffusion problem in a semi-infinite domain (Crank 1980),

$$\overline{f}_{ed} = c_s \left(\frac{D}{\pi t} \right)^{1/2}, \tag{3.1}$$

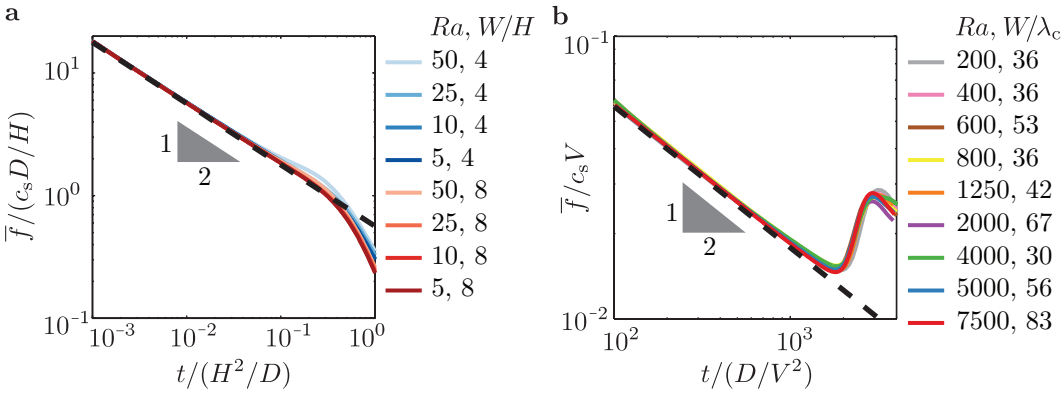

FIGURE 4. During the early diffusion regime, the mean dissolution flux, $\overline{f}$, can be modeled by the flux from a 1D diffusion problem (dashed lines; eq 3.1), provided the source is large enough for edge convection to be negligible. **a.** For $Ra \lesssim 55$, edge convection is negligible provided $W \gtrsim 4H$, and all numerically-measured fluxes (colored) collapse to the diffusion solution. This solution becomes invalid at $t_{\mathrm{ld1}} \sim H^2/D$, when the system transitions to the late diffusion regime. **b.** For $Ra \gtrsim 133$, all numerically-measured fluxes (colored) collapse to the diffusion solution provided $W \gtrsim 30\lambda_{\mathrm{c}}$. The diffusion solution becomes invalid at $t_{\mathrm{f}} \sim D/V^2$, when the system transitions to the fingering regime.

as shown in figure 4 (subscripts on $\overline{f}$ indicate the regime for the remainder of the manuscript).

The diffusion model is valid before the system transitions to the next regime, which depends on the Rayleigh number. For $Ra \lesssim 55$, the next regime is late diffusion and the transition occurs when the diffusion front reaches the bottom of the layer: $t_{\mathrm{ld1}} \sim H^2/D$ (figure 4**a**). For $Ra \gtrsim 133$, the next regime is fingering and the transition occurs at $t_{\mathrm{f}} = \psi D/V^2$, as found in previous studies (Ennis-King *et al.* 2005; Xu *et al.* 2006; Riaz *et al.* 2006; Hassanzadeh *et al.* 2007; Slim & Ramakrishnan 2010). The constant ψ depends on the criterion used to define the onset of fingering. Here, we define the onset as the time when the mean flux reaches a local minimum before rising sharply due to fingering (figure 4**b**). Based on this criterion, we find that $\psi \approx 2000$. For intermediate Rayleigh numbers, $55 \lesssim Ra \lesssim 133$, the subsequent regime is unclear so the transition is not well defined; however, we find that the diffusion solution is valid until a time between t_{ld1} and t_{f}.

Fingering (f). In the fingering regime, CO_2 diffuses into a thin boundary layer that breaks up into sinking fingers. Over the interior of the CO_2 source, this behavior is nearly identical to the fingering process described in previous studies: as the fingers fall, relatively unsaturated water simultaneously rises to the source, which maintains large concentration gradients that increase the dissolution rate compared to the previous regime. Near the edge of the source, however, the unsaturated water comes dominantly from the porous layer outside the source region (figure 5**a**). Since the water does not travel upward between descending fingers to reach the source, it is nearly completely unsaturated, leading to higher dissolution fluxes than in the interior (figure 5**b**). These fluxes are similar in magnitude to those that occur immediately after the onset of fingering, when the dissolution flux reaches a local maximum (Hassanzadeh *et al.* 2007; Slim *et al.* 2013). Directly at the edge, the inflow of water stabilizes a small boundary layer, which can be modeled with the boundary layer solution derived by Cheng & Chang (1976) (figure 5**c**).

For $Ra \gtrsim 2000$, the mean dissolution flux during the fingering regime oscillates, but remains approximately constant in time (figure 5**d**). Since the fluxes near the edge are

larger than those in the interior, the value of the mean flux depends on the size of the CO_2 source. We find that when the source is larger than about $100\lambda_c$, the mean flux converges to

$$\overline{f}_f \approx 0.017 c_s V, \tag{3.2}$$

in agreement with previous results (figure 5**e**) (Hesse 2008; Pau *et al.* 2010; Hidalgo *et al.* 2012). The flux begins to decrease from this value at $t_{sf} \approx 15H/V$, which is the time required for dissolved CO_2 to sink to the bottom in fingers and then recirculate back to the top boundary.

For $133 \lesssim Ra \lesssim 2000$, the flux rises to a peak after the onset of fingering and then continually declines with minor oscillations, as observed in previous work (Hassanzadeh *et al.* 2007). While the flux fails to exhibit a steady state, equation 3.2 provides a lower bound on the flux. Since the flux continually declines, the transition to the next regime is not well defined, but we adopt the transition time for higher Rayleigh numbers ($t_{sf} \approx 15H/V$) and find agreement with numerical results.

Shutdown/fingering (sf). During the shutdown/fingering regime, the source region exhibits three zones of different behavior (figure 6**a**). In the inner zone (iz), dissolved CO_2 sinks to the bottom of the layer in fingers and then recirculates back to the top boundary, where it reduces the concentration gradients and therefore also the dissolution fluxes. This behavior is essentially identical to the convective shutdown behavior observed in closed systems (Hewitt *et al.* 2013; Slim *et al.* 2013). In the *outer zone* (oz), fingering occurs in the unsaturated water that flows in from the porous layer outside the source region. This inflow is the counter-current to the flow of dense, CO_2-rich fluid that migrates away from the source along the bottom of the layer (figure 6**a**). In the *middle zone* (mz), dissolved CO_2 from the outer zone enters from the right and flows to the left along the top part of the layer (figure 6**b**). CO_2 also dissolves via fingering in this zone, but the fingers dominantly remain in the top part of the layer; this is reflected in the observation that the vertical velocities go to zero along the midline of the layer (figure 6**c**). As the flow advances toward the interior, dissolution continues until the concentration rises to values similar to those in the inner zone, at which point the horizontal velocities become very small and the dissolved CO_2 sinks to the bottom. In the bottom part of the layer, the dissolved CO_2 flows to the right as a dense gravity current and eventually leaves the source region.

To model the mean dissolution flux in this regime, we first obtain models for each of the three zones, focusing on high-Ra systems ($Ra \gtrsim 2000$). In the outer zone, the dissolution mechanism is very similar to the previous regime and the mean dissolution flux can be modeled with the previous result (see eq. 3.2):

$$\widetilde{f}_{oz} = \frac{1}{-x_{mz}} \int_{x_{mz}}^{0} f \, dx \approx 0.017 c_s V, \tag{3.3}$$

where the tilde denotes a lateral average over a region of the constant-concentration boundary and subscripts denote the specific region. While the actual flux is slightly higher due to the inflow of nearly completely unsaturated water, we use this value for simplicity and find it to be a reasonable approximation of the numerically measured flux. The outer zone extends over the range $x_{mz} \leqslant x \leqslant 0$, where x_{mz} is the right boundary of the middle zone (figure 6**a**). We find empirically that $x_{mz} \approx -0.3H$, although we currently cannot rule out that x_{mz} might exhibit some dependence on other parameters as well.

In the inner zone, dissolution occurs via the convective shutdown mechanism described by Hewitt *et al.* (2013) and Slim *et al.* (2013), and can be modeled with the formulas

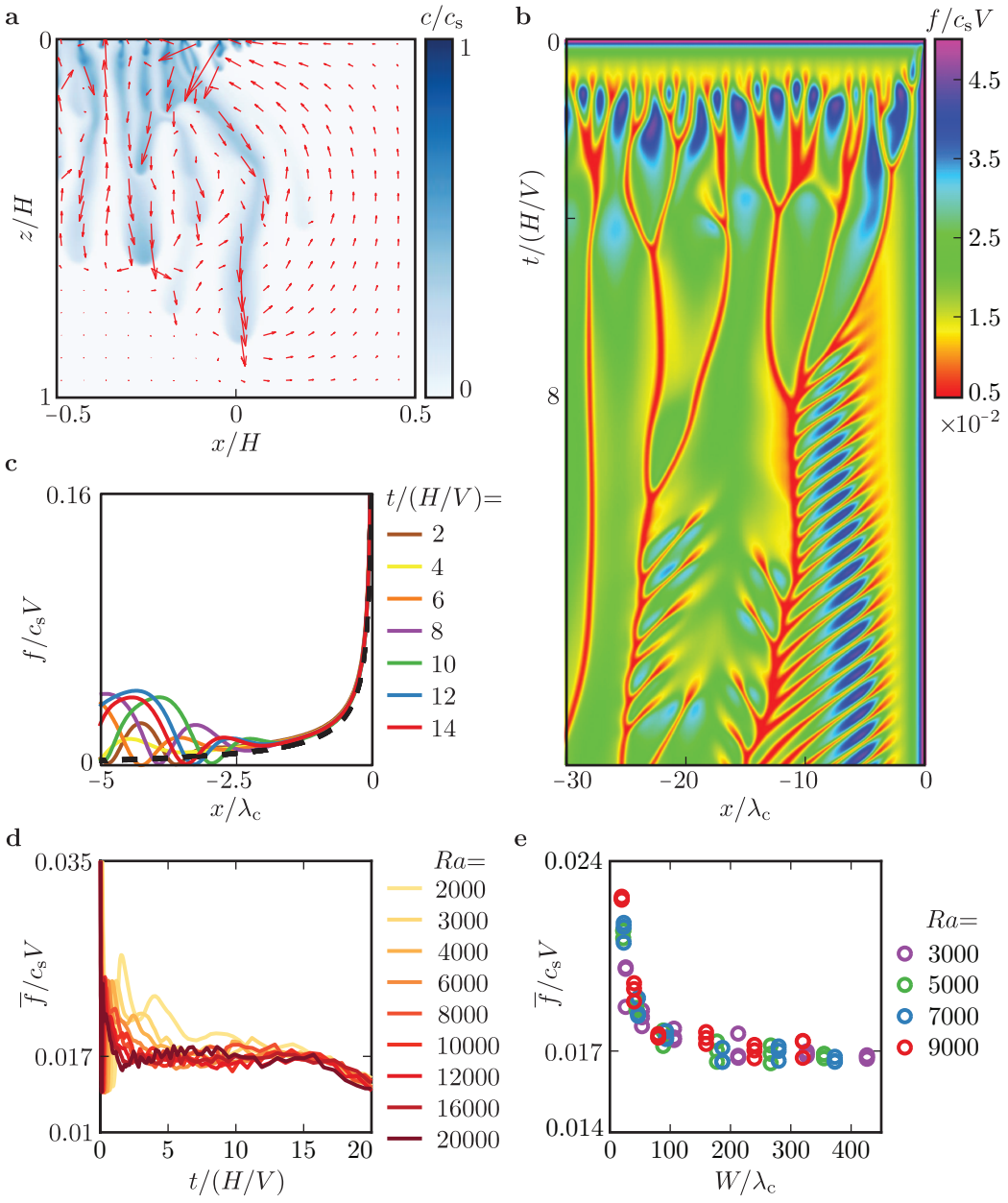

FIGURE 5. During the fingering regime, CO_2-rich fingers fall to the bottom of the layer and fresh water circulates to the source. **a.** Over the interior of the source, the unsaturated water comes from below; at the edge, it comes from the porous layer to the right (shown for $Ra = 10,000$). **b.** The inflow of water from outside the source region sweeps fingers to the interior, as shown by the repetition of diagonal red branches along the right side of the surface plot ($Ra = 10,000$). The blue regions between the branches indicate that the fluxes are higher near the edge than in the interior. **c.** A stable boundary layer exists directly at the edge. Numerical measurements of the flux there (colored) agree with the analytical solution (dashed). **d.** For $Ra \gtrsim 2000$, the mean dissolution flux oscillates but is approximately constant in time ($W \gg 100\lambda_c$). **e.** When the length of the CO_2 source is larger than about $100\lambda_c$, the elevated fluxes near the edge are negligible and the mean flux converges to $\overline{f} \approx 0.017 c_s V$. Different data points for the same value of W/λ_c are different realizations for different random perturbations.

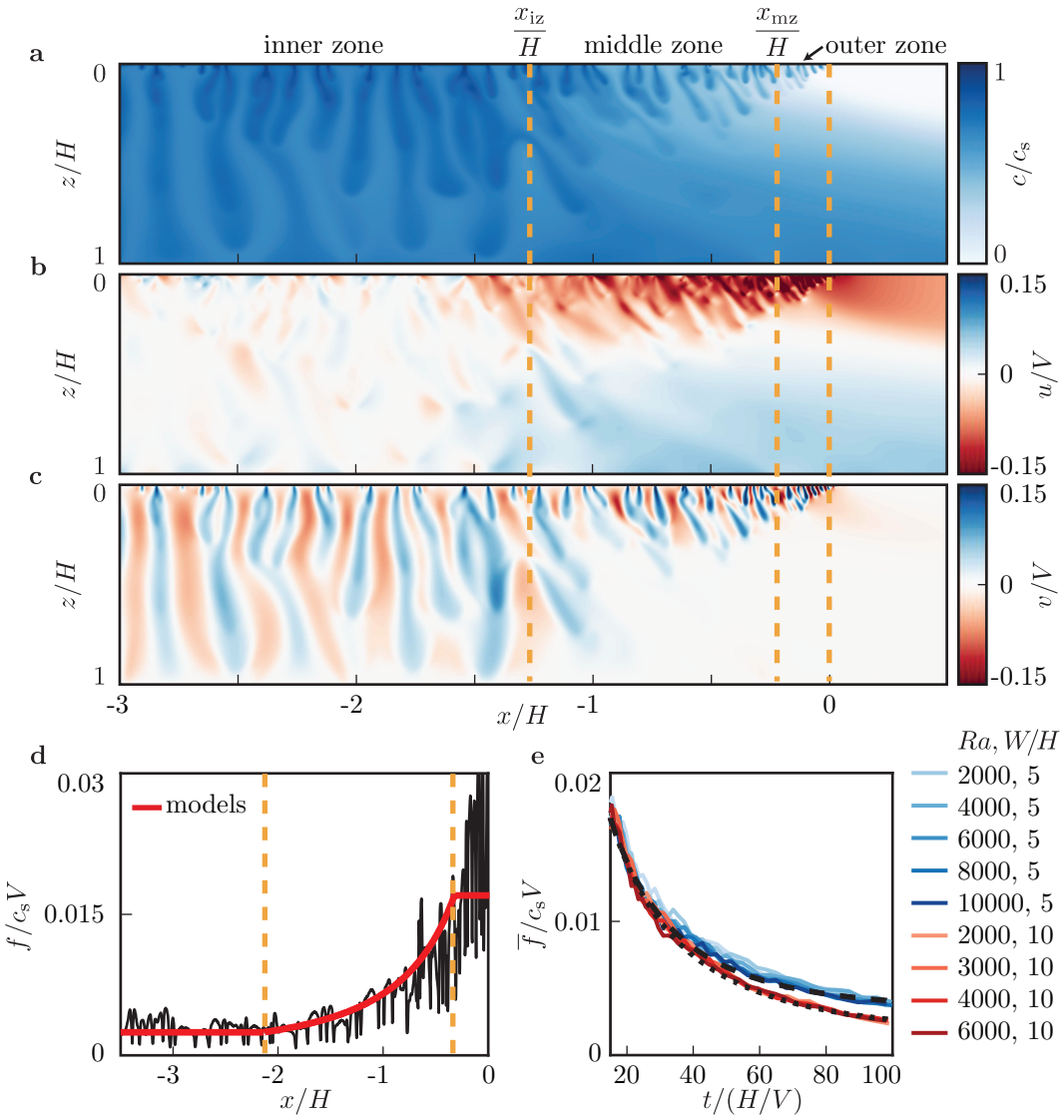

FIGURE 6. In the shutdown/fingering regime, the source region can be divided into three zones as shown by the dashed orange lines. **a.** In the inner zone, dissolution decreases due to the accumulation of dissolved CO_2. In the outer zone, dissolution remains at relatively high rates due to the inflow of unsaturated water along the top of the layer. In the middle zone, the dissolution rate transitions between the neighbouring zones. **b.** The horizontal velocities in the middle zone are dominantly to the left in the upper part of the layer, sweeping dissolved CO_2 toward the interior. In the lower part of the layer, they are dominantly to the right, carrying dissolved CO_2 outside of the source region. **c.** The vertical velocities in the middle zone are large in the upper part of the layer but nearly vanish at the centreline, indicating that fingering is mostly confined to the top. **d.** Analytical models for the dissolution flux in each zone (red; eqs 3.5, 3.8, and 3.2) agree well with numerically-measured fluxes along the source (black). **e.** We average the flux models from each zone to find the mean dissolution flux over the entire source. The averaged model (long dashed: $W = 5H$, short dashed: $W = 10H$; eq 3.10) agrees well with numerical results for $Ra \gtrsim 2000$.

they derived:

$$\overline{\overline{c'}}_{\mathrm{iz}} = \frac{1}{H}\frac{1}{x_{\mathrm{iz}}+W}\int_0^H \int_{-W}^{x_{\mathrm{iz}}} c'\,dx\,dz = 1-(1+\kappa(t-t_0)V/H)^{-1}\,, \tag{3.4}$$

$$\widetilde{f}_{\mathrm{iz}} = \frac{1}{x_{\mathrm{iz}}+W}\int_{-W}^{x_{\mathrm{iz}}} f\,dx = c_{\mathrm{s}}V\kappa\left(1-\overline{\overline{c'}}_{\mathrm{iz}}\right)^2. \tag{3.5}$$

These formulas are box models in that they describe the average behavior of the system over a box-shaped region. In these formulas, $\overline{\overline{c'}}_{\mathrm{iz}}$ is the dimensionless mean concentration in the inner zone (double overbars denote averaging vertically over the entire porous layer and horizontally over a region of the layer, which is indicated by the subscripts), $\widetilde{f}_{\mathrm{iz}}$ is the mean dissolution flux into the inner zone, t_0 is a virtual time origin, and κ is a constant. Slim *et al.* (2013) used the ad hoc value of $\kappa = 0.05$, and Hewitt *et al.* (2013) derived the value to be $\kappa = 0.028$ based on analogy to Rayleigh-Bénard convection; both used $t_0 = 0$. We empirically find that $\kappa = 0.028$ and $t_0 = 5H/V$ provide the best fit to the data.

In the middle zone, we develop a model for the upper part of the layer that couples dissolution due to fingering and horizontal advection. To derive the model, we vertically average the concentration equation (eq 2.3) and make several assumptions. We assume that diffusion is negligible compared to advection outside the boundary layer at $z = 0$, and that the horizontal velocity in the upper part of the layer, u_{mz}, is independent of both x and z. Numerical results show that this is not strictly true, but we find that this simplification captures the general behavior and yields acceptable results. We also assume that the vertical mass flux from the upper part of the layer to the lower part is negligible. This assumption is valid over most of the middle zone since the high CO_2 concentrations in the underlying gravity current cause the vertical velocities to become negligibly small along the midline of the layer (figure 6**c**). The assumption is invalid at the left boundary of the zone were nearly all the dissolved CO_2 sinks to the bottom layer, but we find that this region is small and has a minor impact on the results. Finally, we assume that the dissolution flux can be modeled with the expression from the convective shutdown model, equation 3.5 (with $\overline{\overline{c'}}_{\mathrm{iz}}$ replaced by $\breve{c'}$ below). Since the convective shutdown model is derived via horizontal averaging over several finger widths, this assumption causes our model to capture behavior at the scale of several fingers.

Under these assumptions, we derive an advection equation that incorporates the expression for the dissolution flux from the shutdown model (eq 3.5) as a forcing term:

$$\frac{\partial \breve{c'}}{\partial t} + u_{\mathrm{mz}}\frac{\partial \breve{c'}}{\partial x} = \frac{V\kappa}{\eta}\left(1-\breve{c'}\right)^2, \tag{3.6}$$

where η is the thickness of the upper layer and $\breve{c'} = \eta^{-1}\int_0^\eta c'\,dz$ is the dimensionless concentration vertically averaged over the upper layer (see appendix A for the derivation). This equation states that the mass transported into the upper layer via fingering is swept laterally through the layer via advection. For the boundary condition, we fix the concentration at the right boundary: $\breve{c'}(x = x_{\mathrm{mz}}) = \breve{c'}_{\mathrm{R}}$, where $\breve{c'}_{\mathrm{R}}$ is the vertically averaged concentration that enters from the outer zone. Based on numerical observations, the behavior in the upper layer is essentially time invariant, so we solve the equation at steady state:

$$\breve{c'}_{\mathrm{mz}} = 1-\left(\frac{V\kappa}{u_{\mathrm{mz}}\eta}\left(x-x_{\mathrm{mz}}\right)+\frac{1}{1-\breve{c'}_{\mathrm{R}}}\right)^{-1}, \tag{3.7}$$

$$\widetilde{f}_{\mathrm{mz}} = c_{\mathrm{s}} V \kappa \left(\frac{V\kappa}{u_{\mathrm{mz}}\eta} \left(x - x_{\mathrm{mz}} \right) + \frac{1}{1 - \breve{c}'_{\mathrm{R}}} \right)^{-2}. \tag{3.8}$$

Since the model is a hyperbolic equation, the position of the downstream boundary to the left, x_{iz}, was not required for the solution. We define the location of this boundary *a posteriori* as the point at which the vertically averaged concentration in the middle zone equals the mean concentration in the inner zone. Equating equations 3.4 and 3.7, we find:

$$x_{\mathrm{iz}} = x_{\mathrm{mz}} + \frac{u_{\mathrm{mz}}\eta}{V\kappa} \left(\kappa \left(t - t_0 \right) \frac{V}{H} - \frac{\breve{c}'_{\mathrm{R}}}{1 - \breve{c}'_{\mathrm{R}}} \right). \tag{3.9}$$

Based on this definition, the location of the left boundary continually moves toward the interior as the inner region becomes more saturated, which agrees with observations from the simulations. We set the thickness of the top layer and the velocity empirically from numerical data: $\eta \approx 0.3H$ and $u_{\mathrm{mz}} \approx -0.07V$. We set the mean concentration at the right boundary to ensure continuity of the dissolution flux with the outer zone: $\breve{c}'_{\mathrm{R}} = 1 - (\widetilde{f}_{\mathrm{oz}}/\kappa)^{1/2} \approx 0.22$ (see eq 3.5). This value matches observations from the simulations (figure 6**a**).

We find that, for $Ra \gtrsim 2000$, the dissolution flux at every location along the CO_2 source can be approximated by combining the models for each of the three zones (figure 6**d**). To determine the mean dissolution flux over the source, we average the models:

$$\overline{f}_{\mathrm{sf}} = \frac{1}{W} \left[\int_{-W}^{x_{\mathrm{iz}}} \widetilde{f}_{\mathrm{iz}} dx + \int_{x_{\mathrm{iz}}}^{x_{\mathrm{mz}}} \widetilde{f}_{\mathrm{mz}} dx + \int_{x_{\mathrm{mz}}}^{0} \widetilde{f}_{\mathrm{oz}} dx \right], \tag{3.10}$$

As shown in figure 6**e**, the solution for the mean flux agrees with numerical measurements. The solution becomes inaccurate at $t_{\mathrm{ss}} \approx 100H/V$, when the system transitions to the next regime.

Shutdown/slumping (ss). In the shutdown/slumping regime, the source region exhibits two zones of different behavior (figure 7**a**). In the inner zone (iz), the dissolution mechanism is the same as in the previous regime: convective shutdown. In the outer zone (oz), the mechanism is similar to that in the previous regime: dissolution occurs via fingering into relatively unsaturated fluid that flows in from the layer outside the source region. As before, this flow is the counter current to the dense, CO_2-rich gravity current that slumps away from the source. The difference is that, in this regime, the extent of the gravity current is large relative to the thickness of the layer, and as a result, the flux of CO_2 out of the source region continually decreases with time. Since the outer zone is nearly saturated, this causes the dissolution flux into the outer zone to also continually decrease with time, whereas previously it was constant.

To model dissolution in the outer zone, we develop a box model that relates the mean dissolution flux to the flux into the dense gravity current. To derive the model, we average the concentration equation (eq 2.3) over the outer zone in both the vertical and horizontal directions:

$$\frac{\partial \overline{\overline{c'}}_{\mathrm{oz}}}{\partial t} = \frac{1}{|x_{\mathrm{iz}}|} \left(\widehat{f}(x = x_{\mathrm{iz}}) - \widehat{f}(x = 0) \right) + \frac{1}{H} \widetilde{f}_{\mathrm{oz}}. \tag{3.11}$$

$\overline{\overline{c'}}_{\mathrm{oz}}$ is the dimensionless mean concentration in the outer zone, $\widehat{f}(x = x_{\mathrm{iz}})$ is the mean horizontal mass flux from the inner zone to the outer zone, $\widehat{f}(x = 0)$ is the mean horizontal mass flux from the outer zone into the gravity current, and $\widetilde{f}_{\mathrm{oz}}$ is the mean dissolution flux into the outer zone, as depicted in figure 7**a** (for the remainder of the text, hats denote

vertical averages over the entire layer: *e.g.* $\widehat{f} = H^{-1}\int_0^H f\,dz$). When the accumulation term on the left and the mean flux from the inner zone to the outer zone are negligible, the equation becomes

$$\widetilde{f}_{\mathrm{oz}} = \frac{H}{|x_{\mathrm{iz}}|}\widehat{f}(x=0), \tag{3.12}$$

which states that the mean dissolution flux in the outer zone is directly proportional to the flux into the gravity current. Based on numerical results, we find that the flux from the inner zone to the outer zone is approximately zero when $x_{\mathrm{iz}} \approx 3H$ (figure 7**c**). In contrast to the previous regime, the location of the boundary is fixed in this regime.

To quantify the flux into the gravity current, we model the migration of the current. We assume that vertical velocities in the current are negligible compared to the horizontal velocities (Dupuit approximation), which is justified by the large lateral extent of the current relative to its height in this regime (Bear 1972). We also assume sharp interfaces. Since diffusion is the only mechanism by which mass enters the system, the interface is always diffuse, but we treat it as sharp for simplicity and find agreement with numerical results for high Rayleigh numbers ($Ra \gtrsim 2000$). Under these assumptions, the height of the sharp interface, h, can be modeled by the following equation (Bear 1972; De Josselin De Jong 1981; Huppert & Woods 1995):

$$\frac{\partial h}{\partial t} - V\frac{\partial}{\partial x}\left[h\left(1-\frac{h}{H}\right)\frac{\partial h}{\partial x}\right] = 0, \tag{3.13}$$

where h is measured from the bottom of the layer. We solve this equation in a semi-infinite domain with the left boundary fixed at the right edge of the source region. For the left boundary condition, we set the height of the current at $x = 0$ based on the observation that the current remains pinned at the edge of the source; from numerical observations, the pinned height is $h \approx 0.7H$. We transform the equation into a self-similar form using the similarity variable $\xi_{\mathrm{ss}} = x/(VHt)^{1/2}$, and then integrate it numerically. We find that the solution matches the gravity current in the full, 2D simulations (figure 7**b**). From the solution, we calculate the mass flux into the current to be

$$\widehat{f}(x=0) = \frac{1}{H}\frac{d}{dt}\left(c_{\mathrm{c}}\int_0^{x_{\mathrm{n}}} h\,dx\right) = 0.26c_{\mathrm{c}}\left(\frac{HV}{t}\right)^{1/2}, \tag{3.14}$$

where x_{n} is the rightmost edge of the current at which $h = 0$ and c_{c} is the concentration of the current, which we set empirically to $0.65c_{\mathrm{s}}$. This expression shows that the flux into the gravity current decreases diffusively in time with the scaling $t^{-1/2}$, which is due to the fact that the horizontal velocities in the current decrease diffusively in time. To compare this flux with the flux from pure Fickian diffusion, we divide equation 3.14 by equation 3.1: $\widehat{f}(x=0)/\overline{f}_{\mathrm{ed}} \approx (0.03\pi Ra)^{1/2}$. This expression shows that the enhancement in the dissolution flux due to slumping is proportional to the square root of the Rayleigh number.

To model the mean dissolution flux over the entire source, $\overline{f}_{\mathrm{ss}}$, we average the fluxes from both zones:

$$\begin{aligned}\overline{f}_{\mathrm{ss}} &= \frac{1}{W}\left[\int_{-W}^{x_{\mathrm{iz}}}\widetilde{f}_{\mathrm{iz}}dx + \int_{x_{\mathrm{iz}}}^{0}\widetilde{f}_{\mathrm{oz}}dx\right], \\ &= c_{\mathrm{s}}V\frac{1}{W}\left[(W-3H)\kappa\left(1+\kappa(t-t_0)\frac{V}{H}\right)^{-2} + 0.26H\frac{c_{\mathrm{c}}}{c_{\mathrm{s}}}\left(\frac{H}{Vt}\right)^{1/2}\right].\end{aligned} \tag{3.15}$$

This expression agrees with numerical measurements of the mean flux (figure 7**d**). It be-

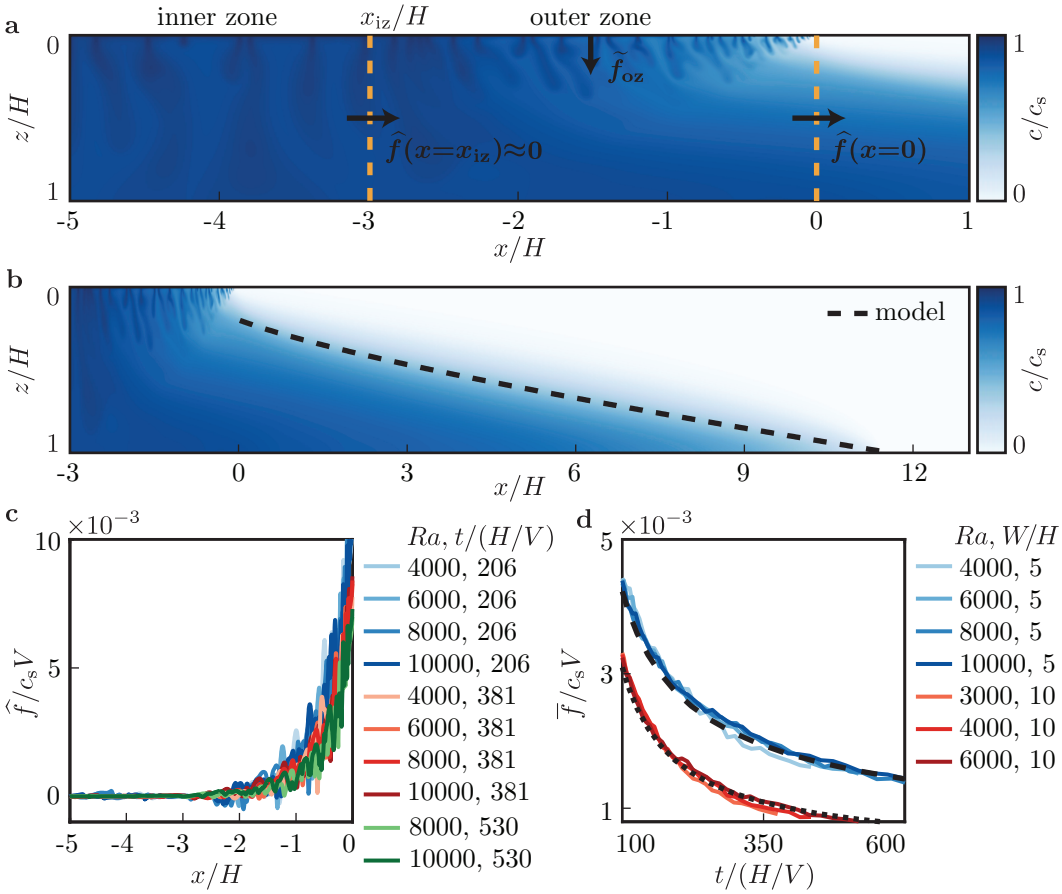

FIGURE 7. **a.** In the shutdown/slumping regime, the source region can be divided into two zones as shown by the dashed orange lines ($Ra = 10,000$). The inner zone is the same as in the previous regime. The flux into the outer zone, $\widetilde{f}_{oz}$, can be modeled from the flux into the dense gravity current, $\widehat{f}(x = 0)$. **b.** The flux into the gravity current can be derived from a sharp-interface model of the current (dashed; eq 3.13), which matches the shape of the current from full, 2D simulations ($Ra = 10,000$). **c.** The flux into the current provides a good approximation of the flux into the outer zone when the flux between the two zones, $\widehat{f}(x = x_{iz})$, is very small. Numerical measurements of the mean horizontal flux, $\widehat{f}$, indicate that this can be achieved by placing the zone boundary at $x_{iz} \approx -3H$. **d.** The model for the mean dissolution flux over the entire source (short dashed: $W = 10H$, long dashed: $W = 5H$; eq 3.15) agrees with numerical results (colored). Data are truncated at the onset of the next regime for clarity.

comes invalid at $t_{sT} \approx 6(H^3/VD)^{1/2}$, when the system transitions to the shutdown/Taylor slumping regime.

Shutdown/Taylor slumping (sT). In the shutdown/Taylor slumping regime, the source region can be divided into the same two zones present in the previous regime. The inner zone is exactly the same, with dissolution occurring via convective shutdown. The outer zone exhibits similar behavior to the previous regime in that the dissolution rate is limited by rate at which CO_2-rich fluid can slump away from the source region as a dense gravity current. It differs, however, in the nature of the gravity current. Whereas previously advection dominated diffusion, in this regime diffusion becomes equally important and a broad transition zone develops between the dense current and the over-riding

counter-current (figure 2). As a result of diffusive mixing, the current decelerates faster than in the previous regime, and consequently the flux of CO_2 out of the source region also decreases faster. A complementary interpretation is that the dissolution flux decreases faster because the counter-current no longer supplies nearly unsaturated fluid to the source region, but rather fluid with high saturations of CO_2 originating from the dense gravity current.

To model the dissolution flux in the outer zone, we employ the box model from the previous regime that relates the dissolution flux to the flux into the dense gravity current (eq 3.12). However, to model the flux into the current, we now use a model that captures diffusive mixing between the dense current and the counter-current. The model, called the Taylor slumping model, is a partial differential equation for the vertically averaged concentration in the porous layer, $\overline{c}$ (Szulczewski & Juanes 2013):

$$\frac{\partial \widehat{c}}{\partial t} - D\frac{\partial^2 \widehat{c}}{\partial x^2} - \frac{\partial}{\partial x}\left(\frac{H^4 V^2}{120 D c_s^2}\left[\frac{\partial \widehat{c}}{\partial x}\right]^2 \frac{\partial \widehat{c}}{\partial x}\right) = 0. \tag{3.16}$$

The middle term in this equation is a Fickian diffusion term. The rightmost term can be interpreted as a nonlinear diffusion term that captures the coupling between Taylor dispersion at the aquifer scale and the reduction in lateral concentration gradients that drive flow (Szulczewski & Juanes 2013). Scaling these terms shows that the Fickian diffusion term is negligible compared to the nonlinear term when the aspect ratio of the current is small relative to the Rayleigh number: $L/H \ll Ra/\sqrt{120}$, where L is the lateral extent of the current. As a result, the nonlinear term dominates at early times before the current becomes too large, and we neglect the Fickian diffusion term until the last regime.

We solve the Taylor slumping equation in a semi-infinite domain with the left boundary at the right edge of the source region. For the boundary condition, we fix the vertically averaged concentration to the completely saturated concentration ($\widehat{c}(x=0) = c_s$). While a more rigorous boundary condition could be based on the time-evolving concentration at the boundary—which could be estimated by the convective shutdown solution in the inner zone—the simple condition we impose is reasonable since the actual dimensionless concentration at the boundary is close to unity at times for which the Taylor slumping model is valid. The error introduced by this simplification decreases with time as the source region approaches saturation.

The simplified boundary condition permits the Taylor slumping model to be solved analytically via a similarity solution in the variable $\xi_{Ts} = x/(H^4V^2t/120D)^{1/4}$:

$$\frac{\widehat{c}}{c_s} = 1 - \frac{1}{2\sqrt{12}}\left[\xi_{Ts}\left(\alpha^2 - \xi_{Ts}^2\right)^{1/2} + \alpha^2 \arcsin\left(\frac{\xi_{Ts}}{\alpha}\right)\right], \tag{3.17}$$

where $\alpha = (198/\pi^2)^{1/4}$. This solution agrees with numerical measurements of the vertically averaged concentration. The agreement improves over time since the model is asymptotic (Szulczewski & Juanes 2013), and since the boundary condition becomes increasingly accurate with time (figure 8**a**). From the solution, we find the flux into the current:

$$\widehat{f}(x=0) = \frac{1}{H}\frac{d}{dt}\left(H\int_0^\infty \widehat{c}\, dx\right) = c_s\left(\frac{8}{405\pi^6}\right)^{1/4}\left(\frac{H^4V^2}{Dt^3}\right)^{1/4}. \tag{3.18}$$

This equation agrees with the numerically measured fluxes out of the source region (figure 8**b**). It shows that, in contrast to the previous regime, the flux into the gravity current decreases sub-diffusively. We find empirically that equation 3.18 becomes valid at

time $t_{\mathrm{sT}} \approx 6(T_{\mathrm{A}}T_{\mathrm{D}})^{1/2} = 6(H^3/VD)^{1/2}$, where $T_{\mathrm{A}} = H/V$ is the characteristic advection time across the layer and $T_{\mathrm{D}} = H^2/D$ is the characteristic diffusion time across the layer. While the precise physical origin of this scaling is unclear, the dependence on both advection and diffusion timescales is reasonable since the model couples advection and diffusion.

While the convective shutdown mechanism continues to operate in the inner zone, we use an extended form of model from the previous regimes. The extended model captures behavior at low Rayleigh numbers and long times more accurately than the previous model. It was derived by Hewitt *et al.* (2013):

$$\overline{\overline{c'}}_{\mathrm{iz}} = 1 - \gamma\left[(1+\gamma)e^{\kappa\gamma(t-t_0)V/H} - 1\right]^{-1}, \tag{3.19}$$

$$\widetilde{f}_{\mathrm{iz}} = c_{\mathrm{s}}V\kappa\left[\left(1-\overline{\overline{c'}}_{\mathrm{iz}}\right)^2 + \gamma\left(1-\overline{\overline{c'}}_{\mathrm{iz}}\right)\right], \tag{3.20}$$

where $\gamma = \beta/\kappa Ra$ and $\beta = 2.75$. The previously used model can be derived from this model when $\gamma \ll 1$. As with the previous model, this model agrees with numerical measurements of the dissolution flux in the inner zone (figure 8**c**).

To determine the mean dissolution flux over the source region, we average the fluxes in the inner and outer zones. The flux into the inner zone is given by the extended convective shutdown model (eq 3.20). The flux into the outer zone is given by combining the box model (eq 3.12) with the expression for the flux into the gravity current (eq 3.18). For the left boundary of the box model, $x_{\mathrm{iz}} \approx -3H$ as in the previous regime. The mean dissolution flux is then

$$\begin{aligned}\overline{f}_{\mathrm{sT}} &= \frac{1}{W}\left(\int_{-W}^{x_{\mathrm{iz}}} \widetilde{f}_{\mathrm{iz}}dx + \int_{x_{\mathrm{iz}}}^{0} \widetilde{f}_{\mathrm{oz}}dx\right), \\ &= \frac{1}{W}\left[(W-3H)\widetilde{f}_{\mathrm{iz}} + c_{\mathrm{s}}H\left(\frac{8}{405\pi^6}\right)^{1/4}\left(\frac{H^4V^2}{Dt^3}\right)^{1/4}\right],\end{aligned} \tag{3.21}$$

where $\widetilde{f}_{\mathrm{iz}}$ is given by eq 3.20. This expression agrees with numerically measured fluxes. The agreement improves for larger Rayleigh numbers because the shutdown model becomes more accurate for larger Rayleigh numbers. The agreement also improves with time as the Taylor slumping model becomes more accurate (figure 8**d**).

This validity of equation 3.21 is limited by the late-time validity of the convective shutdown model. We estimate the time at which the convective shutdown model becomes invalid as the time when the effective Rayleigh number, Ra_{e}, decreases to the critical value required for convection, Ra_{c}. The effective Rayleigh number is based on the density difference between the saturated upper boundary and the fluid in the porous layer, and as a result, is a function of the mean concentration in the layer. Following Hewitt *et al.* (2013), we define the effective Rayleigh number as $Ra_{\mathrm{e}} = 4Ra(1-\overline{\overline{c'}}_{\mathrm{iz}})$. We take the critical Rayleigh number to be $Ra_{\mathrm{c}} = 4\pi^2$, which is the appropriate value for a Rayleigh-Bénard flow (Nield & Bejan 2013). We choose this value because the derivation of Hewitt *et al.* (2013) is based on an analogy to Rayleigh-Bénard flow, but the choice may be interpreted as *ad hoc* since the analogy breaks down before this critical value is reached. Solving for the time at which $Ra_{\mathrm{e}} = Ra_{\mathrm{c}}$ yields $t_{\mathrm{Ts}} = (H^2/D)(1/\beta)\ln[(4\beta/\kappa Ra_{\mathrm{c}})(1+\gamma)^{-1}]$, which in the limit of large Ra ($\gamma \ll 1$) becomes $t_{\mathrm{Ts}} \approx H^2/D$. Comparing the convective shutdown model to numerical results confirms the scaling but suggests the prefactor may be slightly larger than one (figure 8**c**).

Taylor slumping (Ts). After time $t_{\mathrm{Ts}} \approx H^2/D$, the interior of the source region

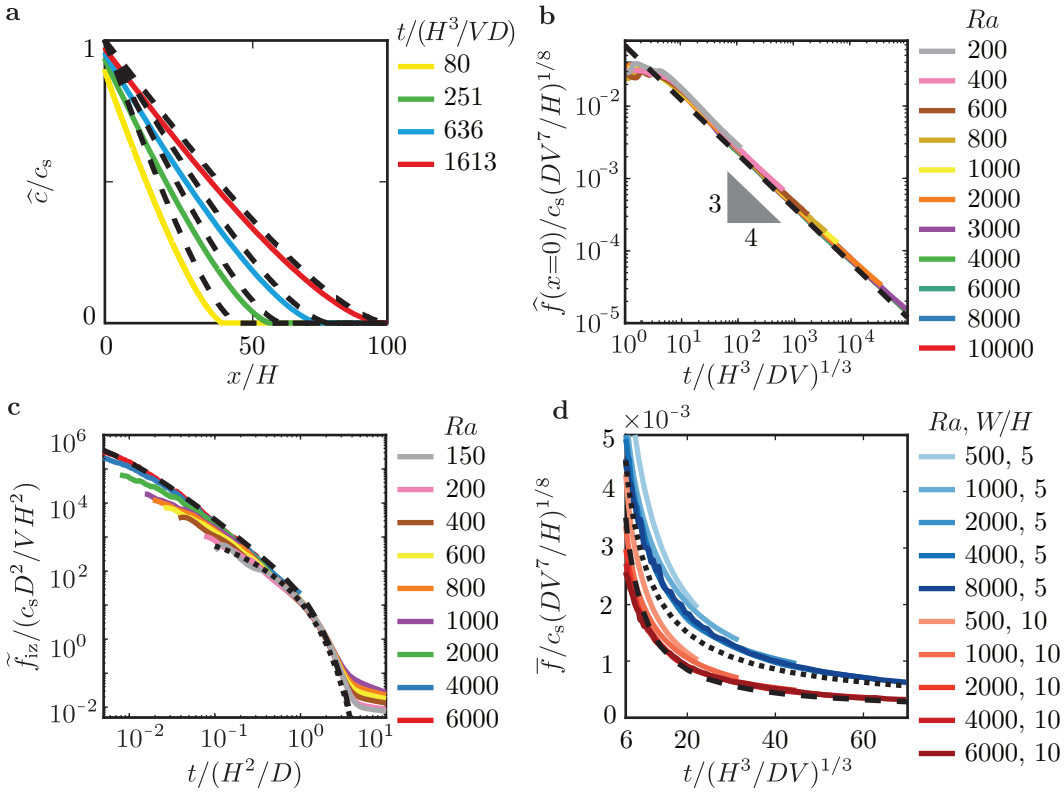

FIGURE 8. **a.** In the shutdown/Taylor slumping regime, the dissolution flux into the outer zone is controlled by the flux into a diffuse gravity current, which we model with the Taylor slumping model (eq 3.16). The model results for the vertically averaged concentration in the layer (dashed; eq 3.17) agree with numerical measurements (colored), particularly at late times. **b.** The model results for the flux into the gravity current (dashed; eq 3.18) agree with numerical measurements of the flux (colored) exiting the source region (all data for $W \geqslant 3H$). Data are truncated at the transition to the next regime for clarity. The simultaneous convergence of all data to the model indicates that the onset time of Taylor slumping scales as $t_{sT} \sim (H^3/VD)^{1/2}$, which is the onset of the shutdown/Taylor slumping regime. **c.** In the inner zone, dissolution continues to occur via convective shutdown. In this regime, we use an extended form of the shutdown model (long dashed: $Ra = 6000$, short dashed: $Ra = 150$; eq 3.20), which describes the numerical fluxes (colored) for $Ra \gtrsim 133$ until $t_{Ts} \sim H^2/D$, when the system transitions to the next regime. **d.** The model for the mean dissolution flux from the entire source (long dashed: $Ra = 6000, W = 10H$, short dashed: $Ra = 8000, W = 5H$; eq 3.21) agrees with numerical measurements (colored), particularly for large times and Rayleigh numbers. Again, data are truncated at the transition to the next regime for clarity.

is essentially completely saturated with CO_2 and convection becomes negligible there (figure 2). At the edge, convection slows but continues to enhance dissolution via the inflow of water with relatively low CO_2 concentrations from the layer outside the source region. This behavior is exactly the same as in the previous regime, but the concentrations in the inflow are higher since the dense gravity current is now longer.

To model the mean dissolution flux in this regime, we use a box model that spans the entire source region. As in the previous two regimes, the model relates the dissolution flux to the flux from the edge of the source into the layer. To model the flux into the layer, we again use the result from the Taylor slumping model (eq 3.18). The mean dissolution

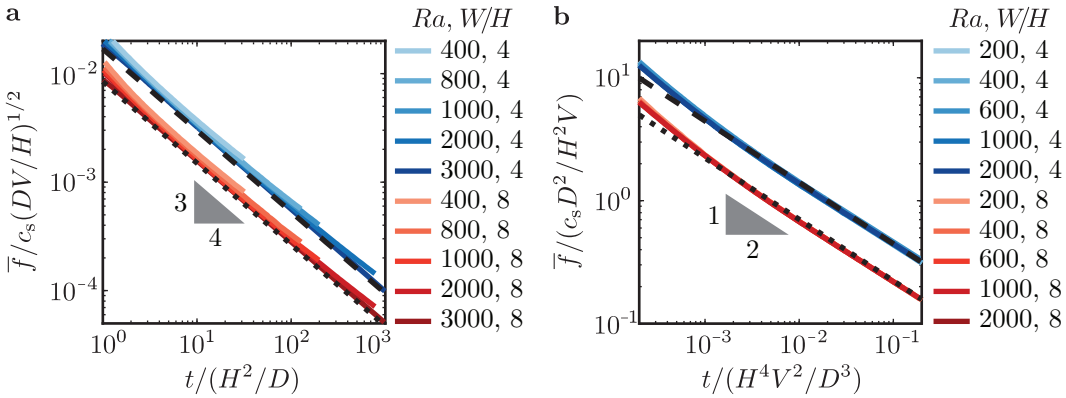

FIGURE 9. In the last two regimes, Taylor slumping and late diffusion, we model the mean dissolution flux using only the horizontal flux out of the source region. **a.** Numerical measurements of the dissolution flux (colored) in the Taylor slumping regime agree with the model (long dashed: $W = 4H$, short dashed: $W = 8H$; eq 3.22). The data are truncated at the onset of the next regime for clarity. **b.** Numerical measurements of the dissolution flux (colored) in the late diffusion regime also agree with our model (long dashed: $W = 4H$, short dashed: $W = 8H$; eq 3.24). The simultaneous convergence of numerical results to the model indicates that, for $Ra \gtrsim 133$, the onset time of late diffusion scales as $t_{ld2} \sim H^4V^2/D^3$.

flux is:

$$\overline{f}_{Ts} = \frac{H}{W}\widehat{f}(x=0) = c_s \frac{H}{W}\left(\frac{8}{405\pi^6}\right)^{1/4}\left(\frac{H^4V^2}{Dt^3}\right)^{1/4}. \tag{3.22}$$

This equation represents a lower bound on the dissolution flux since it assumes that the accumulation of CO_2 in the entire source region is negligible. In practice, the accumulation is non-zero, but approaches zero with time as the layer becomes completely saturated. The equation agrees with numerical results (figure 9**a**).

Late diffusion (ld). At the latest times, convection is negligible relative to diffusion over the entire domain. The dominant dissolution mechanism is diffusion without convective enhancement at the edge of the source, and the dominant transport mechanism outside the source region is lateral diffusion through the porous layer. For high Rayleigh numbers ($Ra \gtrsim 133$), this behavior occurs when the dense gravity current that transports CO_2 away from the source becomes very long. When the current becomes long, the horizontal density gradient that drives the flow becomes very small and, as a result, the velocity becomes very small. The relationship between the lateral velocity, u, and the gradient of vertically-averaged density, $\widehat{\rho}$, is

$$u(z) = \frac{gkH}{\phi\mu}\frac{\partial\widehat{\rho}}{\partial x}\left(\frac{1}{2} - \frac{z}{H}\right) + O(\epsilon^2), \tag{3.23}$$

where $\epsilon = H/L$ and L is the horizontal extent of the flow (Szulczewski & Juanes 2013). By equating the flux from lateral diffusion (eq 3.24) with the flux from Taylor slumping (eq 3.22), we find the time at which diffusion dominates to be $t_{ld2} = (8/405\pi^4)(H^4V^2/D^3)$.

For lower Rayleigh numbers, the transition to dissolution via lateral diffusion occurs at a different time. For $Ra \lesssim 55$, the previous regime is early diffusion, in which dissolution occurs dominantly via diffusion in the vertical direction without convective enhancement. When vertical diffusion is the preceding mechanism, the transition occurs when the diffusion front reaches the bottom of the layer at $t_{ld1} \approx H^2/D$, as discussed previously.

To model the dissolution flux, we use a box model that spans the entire source region as in the previous regime. To model the lateral flux out of the source region, we use the flux from a 1D diffusion problem in a semi-infinite domain. The mean dissolution flux is then:

$$\overline{f}_{\mathrm{ld}} = \frac{H}{W}\widehat{f}(x=0) = \frac{H}{W}c_{\mathrm{s}}\left(\frac{D}{\pi t}\right)^{1/2}. \tag{3.24}$$

This is the same equation as for the first regime (eq 3.1), but with an additional dependence on the ratio of the layer thickness, H, to the width of the source, W. This dependence arises because we are calculating the flux as the rate of mass transfer vertically through the CO_2-brine interface, but the flux in this regime is actually constrained by the rate of mass transfer laterally through the porous layer. This solution agrees with numerically measured dissolution fluxes (figure 9**b**).

4. Summary of regimes

We classify dissolution into seven regimes. In the early diffusion regime, dissolution occurs dominantly via diffusion without convective enhancement. In the fingering regime, dense, CO_2-rich fluid sinks away from the source in fingers while relatively unsaturated fluid rises upward, leading to an elevated dissolution flux that is approximately constant in time. In the shutdown/fingering regime, the inner zone of the source region undergoes convective shutdown, in which the dissolution rate slows due to the recirculation of CO_2-rich fluid from the fingers back up to the source; the outer zone continues to exhibit fingering in a return flow of nearly fresh water from the porous layer outside the source region. In the shutdown/slumping and shutdown/Taylor slumping regimes, convective shutdown continues in the inner zone, while dissolution in the outer zone is constrained by the rate at which CO_2-rich fluid can migrate away from the source as a gravity current. This gravity current exhibits a sharp boundary with the over-riding counter current in the shutdown/slumping regime, and the dissolution flux in the outer zone decreases diffusively in time. However, in the shutdown/Taylor slumping regime, the boundary becomes highly diffuse and the dissolution flux in the outer zone decreases sub-diffusively in time. In the Taylor slumping regime, dissolution at the edge continues to be limited by the migration of a diffuse gravity current, but convective shutdown ceases in the inner zone due to nearly complete saturation of the layer. Finally, in the late diffusion regime, dissolution occurs via lateral diffusion though the porous layer with negligible convection.

All of the regimes can be organized into the phase diagram in figure 10. This diagram shows that the occurrence of the regimes depends on the Rayleigh number. For the highest Rayleigh numbers ($Ra \gtrsim 2000$), all regimes occur: dissolution begins in the early diffusion regime, then transitions through the fingering regime, the three regimes with convective shutdown, the Taylor slumping regime, and finally the late diffusion regime. For smaller Rayleigh numbers, fewer regimes occur as convection becomes increasingly less important relative to diffusion. For the smallest Rayleigh numbers ($Ra \lesssim 55$), none of the regimes with convective enhancement occur: dissolution begins in the early diffusion regime and transitions directly to the late diffusion regime.

5. Application

Since all the models have been derived for an idealized system, their applicability to real geologic traps is uncertain. While our system is 2D, rectilinear, perfectly horizon-

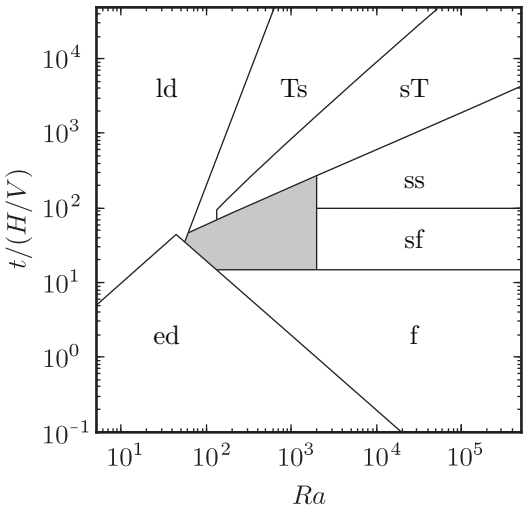

FIGURE 10. Phase diagram of the dissolution regimes. Tracing a vertical line through the diagram illustrates the regimes that occur for a particular Rayleigh number. The gray region in the center represents conditions for which we did not model dissolution. The sharp angle on the border between the Taylor slumping (Ts) and shutdown/Tayor slumping (sT) regimes occurs at $Ra = 133$, the leftmost extent of the fingering regime (f), due to uncertainty about the validity of the convective shutdown mechanism for lower Rayleigh numbers.

tal, and homogeneous, real geologic traps typically exhibit complex 3D geometries and heterogeneity at a variety of scales due to features such as lenses and layers of fine-grained rock. In addition, the length of the CO_2-brine interface in a real trap continually decreases as the CO_2 dissolves, whereas the interface length in our system is constant (figure 1). Due to the large number of differences and their complexity, we can not at this stage rigorously evaluate the accuracy of our models in real traps or determine whether they provide upper or lower bounds on the dissolution rates. Some features of real traps, such as slope and natural groundwater flow, will likely lead to higher dissolution rates in practice, but the effect of other features such as heterogeneity is more difficult to predict. Consequently, we emphasize that the main contribution of the study is, strictly speaking, the elucidation of how dissolution is affected by the finite CO_2-brine interface that exists during storage in geologic traps.

While our models are based on several assumptions, applying them to real geologic traps can be useful. Since the models are all analytical, they can quickly provide rough estimates of the dissolution rates that can be expected in practice, and can help constrain the time required to completely dissolve a volume of injected CO_2. While highly uncertain, these estimates are useful because there are currently several sequestration projects worldwide either injecting or planning to inject CO_2 into structural and stratigraphic traps, but there are limited techniques available to quickly predict dissolution rates over the lifetime of the project. While large simulations incorporating site-specific geometry and geology play an important role in quantifying these rates, they are time-consuming to develop and the information they provide is also highly uncertain due to uncertainty in the subsurface properties. In addition, uncertainty arises from the inability of conventional simulations to resolve the small length scales associated with the fingering instability, which plays a key role in the dissolution process.

With their limitations in mind, we apply the models to a few simplified geologic traps. The traps are characterized by six dimensional parameters: the layer thickness, H; the

trap type	**thickness** H [m]	**permeability** k [mD]	Ra
thick, high perm.	200	1000	2×10^5
thin, high perm.	20	1000	2×10^4
thick, low perm.	200	10	2×10^3
thin, low perm.	20	10	2×10^2

TABLE 1. We apply the dissolution models to four types of simplified geologic traps.

width of the CO_2-brine interface, W; the length of the trap in the $\hat{y}$-direction, L (see figure 1); the CO_2 diffusivity, D; the saturated CO_2 concentration, c_s; and the buoyancy velocity, $V = \Delta\rho g k/\mu\phi$. We set the parameters to represent a range of conditions that may be encountered in the subsurface (Szulczewski *et al.* 2012; Michael *et al.* 2010). While all of these parameters exhibit variability, for simplicity we set most of them to fixed values: $L = 40$ km, $D = 1 \times 10^{-9}$ m^2/s, $\Delta\rho = 10$ kg/m^3, $\mu = 0.6$ mPa s, $\phi = 0.15$, and $c_s = 50$ kg/m^3. For the layer thickness and permeability, two of the most highly variable parameters, we consider low and high values: for the layer thickness, we consider $H = 20$ m and $H = 200$ m, and for the permeability, we consider $k = 10$ mD and $k = 1000$ mD (1 mD $\approx 10^{-15}$ m^2). These permeabilities lead to two buoyancy velocities: 0.3 m/yr and 30 m/yr, respectively. Combining the buoyancy velocities and layer thicknesses yields the four simple traps shown in table 1. For each trap, we consider two values for the width of the CO_2-brine interface: $W = 5$ km and $W = 15$ km.

While the traps are idealizations, they reflect properties from real sequestration projects. The thin, low-permeability trap displays similarities to the upper zones in the Nagaoka project ($H \approx 10$ m, $k \approx 10$ mD) (Mito *et al.* 2013), and the B-sandstone in the Tensleep Formation in the Teapot Dome ($H \approx 30$ m, $k \approx 30$ mD) (Chiaramonte *et al.* 2008). The thin, high-permeability trap displays similarities to the Naylor Field in the CO2CRC Otway Project ($H \approx 25$ m, $k \approx 700$ mD) (Underschultz *et al.* 2011), and the thick, low-permeability trap exhibits properties similar to the Mt. Simon Sandstone in the Cincinnatti Arch ($H \approx 100$ m, $k \approx 10 - 200$ mD) (Michael *et al.* 2010). The thick, high-permeability trap has properties similar to the Utsira Formation in the Sleipner Project ($H \approx 250$ m, $k \approx 5000$ mD), which is not a structural or stratigraphic trap, but is often used to contextualize results of CO_2 dissolution models (Neufeld *et al.* 2010; Hewitt *et al.* 2013; MacMinn & Juanes 2013).

For each idealized trap, we calculate the dissolution flux over ten million years. For most of the traps, the models completely specify the behavior. However, for the thin, low-permeability trap ($Ra = 200$), there is a period of time for which we did not develop models (see figure 10). For these times, we approximate the dissolution flux with a straight line in log space that connects the models we do have; this approximation is a power law in linear space.

The results show a few similarities between the traps, but several differences. The traps are similar in that they all exhibit monotonic decreases in the dissolution flux: the flux first decreases diffusively in the early diffusion regime, becomes constant during the fingering regime, declines sharply in the regimes with convective shutdown, and then decreases more slowly but still sub-diffusively during the Taylor slumping regime (figure 11**a**). However, the detailed trajectories of the fluxes are very different among the traps, with the durations of the different regimes and the magnitude of the fluxes during those regimes varying by orders of magnitude (figure 11**b**). For example, in the high-permeability traps, fingering occurs after about 20 days and the dissolution flux is about

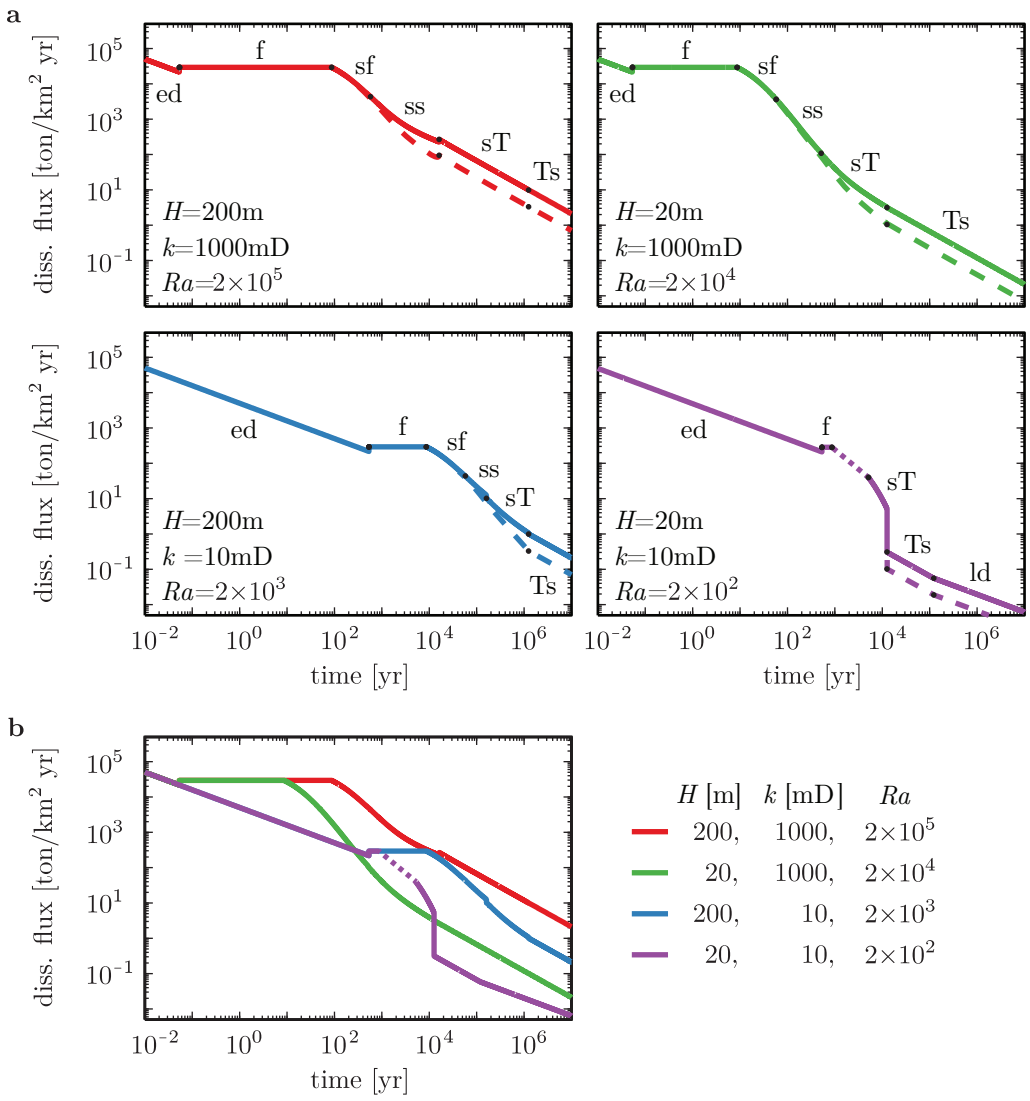

FIGURE 11. We use the simplified models to calculate the evolution of the dissolution flux in four idealized geologic traps characterized in table 1. The short dashed line on the purple curve marks the time period we did not explicitly model, but that we approximate. The steep drop in the purple curve is due to the fact that the model for the Taylor slumping regime (Ts) represents a lower bound on the flux. **a.** The fluxes in each trap exhibit the same general trend: a monotonic decrease, with a period of constant flux during the fingering regime (f). In addition, the wide traps (dashed; W = 15 km) exhibit lower fluxes at late times compared to the narrow traps (solid; W = 5 km). However, the detailed trajectories for each trap exhibit several differences, such as orders of magnitude variation in the transition times between the regimes (black circles) and the magnitude of the flux during the regimes. **b.** These discrepancies are highlighted by comparing the trajectories on the same plot (W = 5 km).

30 kton/km^2/yr (all tons are metric tons), but in the low-permeability traps fingering occurs after about 600 years and the flux is roughly 300 ton/km^2/yr. The time at which the regimes with convective shutdown and gravity currents occur is different for each trap: it ranges from 10 years in the thin, high-permeability trap to about 10,000 years in

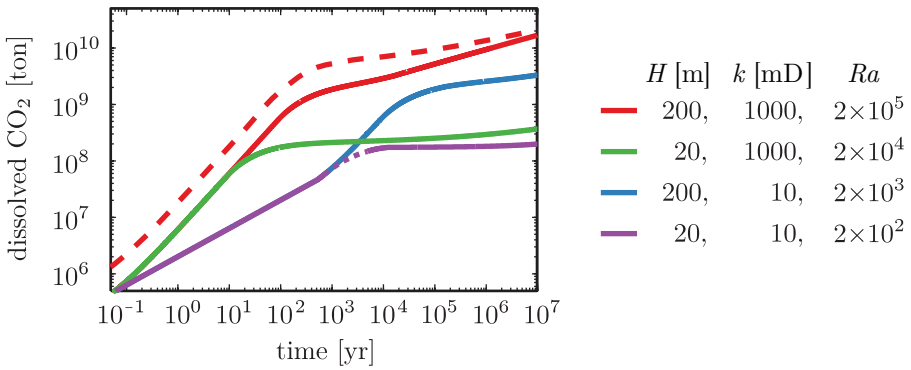

FIGURE 12. For each idealized trap, we integrate the dissolution flux to calculate the dissolved mass of CO_2 vs. time (solid: $W = 5$ km; dashed: $W = 15$ km). The high-permeability traps (red, green) dissolve more CO_2 at short times compared to the low-permeability traps (blue, purple). At late time, however, the quantity of dissolved CO_2 depends on the trap thickness: the thick traps (red, blue) ultimately dissolve more than the thin traps (green, purple). In all traps, large interface widths (large Ws) lead to more dissolved CO_2 for all times we consider (we only show one example for clarity). Comparison to figure 11 shows the opposite effect on the flux.

the thick, low-permeability trap. The magnitude of the fluxes during these regimes also vary widely among the traps.

By integrating the dissolution fluxes, we calculate the cumulative mass of CO_2 dissolved over time in each trap (figure 12). In practice, this quantity is of course constrained by the storage capacity of the trap, but in our idealized model the storage capacity is undetermined because the trap geometry is not fully specified. We find that at early times, the high-permeability traps dissolve more CO_2 than the low-permeability traps due to both the shorter onset time for the fingering regime ($t_f \sim D/V^2$) and the larger magnitude of the flux during the regime ($\overline{f}_f = 0.017 c_s V$). These traps dissolve hundreds of megatons of CO_2 over tens of years, whereas the low-permeability traps barely exceed 10 megatons. At late times, the dissolved mass of CO_2 depends on both the permeability and trap thickness, since the thickness impacts the end of fingering and the subsequent regimes. The thin traps nearly plateau at a little over 100 megatons of CO_2, while the thick traps reach over 1 billion tons—about half the annual emissions of coal- and gas-fired power plants in the US (US Energy Information Administration, US Department of Energy 2009). In all traps, the amount of dissolved CO_2 increases after the end of fingering, though this behavior is negligible in the thin, low-permeability trap and is most pronounced in the thick, high-permeability trap.

While the width of the CO_2-brine interface in our models is constant, the results illustrate that this parameter has a complex effect on dissolution. For the large interface width ($W = 15$ km), the mean dissolution flux is always lower at late times than for the small width ($W = 5$ km) (figure 11**a**). This is due to the fact that, for small W, the relatively large dissolution rates in the outer zone have a stronger impact on the mean behavior. The results for the cumulative CO_2 dissolution, however, exhibit the opposite trend: in all of the traps, the larger interface width leads to the most dissolution for all times up to 10 million years (figure 12). This indicates that increased surface area over which dissolution occurs at early times is more important than the increased dissolution fluxes at the edge at late times. In an actual geologic trap in which the interface width

continually decreases, both the early-time advantage of large surface areas and the late time advantage of relatively large edge-zones will likely exist.

6. Discussion and conclusion

We find that CO_2 dissolution in a geologic trap varies both spatially and temporally. In general, the CO_2 source region exhibits at least two zones of different behavior: an outer zone adjacent to the edge of the source, and an inner zone far away from the edge. In the inner zone, the dissolution mechanisms are nearly identical to those observed in closed systems. Dissolution first occurs via vertical diffusion without convective enhancement, then via fingering, and then via convective shutdown. In the outer zone, however, the mechanisms are strongly impacted by the porous layer outside the source region, which continues to supply relatively unsaturated water long after the inner zone becomes highly saturated. During the fingering and shutdown/fingering regimes, this influx of unsaturated water is approximately constant in time, and as a result, the dissolution flux near the edge is also constant. During the shutdown/slumping regime, the influx of water and dissolution flux decrease diffusively with time due to the migration of dense, CO_2-rich flow away from the source as a gravity current. During the shutdown/Taylor-slumping and Taylor slumping regimes, the influx of water and dissolution flux decrease sub-diffusively in time due to diffusive mixing between the dense gravity current and the low-concentration counter-current. At the latest times, convection becomes negligible relative to diffusion and the dissolution flux becomes limited by lateral diffusion though the porous layer.

Applying the regime models to several representative geologic traps informs the relative importance of the different regimes and provides rough estimates of how much CO_2 may be dissolved in practice. In general, we find that the onset times of the regimes and the magnitudes of the dissolution flux depends strongly on the reservoir properties. This result indicates that there is no typical dissolution behavior and suggests that accurately quantifying dissolution requires a site-specific approach. In addition, it encourages the use of dissolution models in the site-selection process, since a well-chosen site could potentially dissolve hundreds of megatons of CO_2 within tens of years.

Appendix A. Middle zone during shutdown/fingering regime

To derive the model for the middle zone in the shutdown/fingering regime (eq 3.6), we first vertically average the concentration equation over the thickness of the upper part of the layer, η:

$$\frac{\partial \breve{c}}{\partial t} + \frac{\partial}{\partial x}\breve{uc} + \frac{1}{\eta}\left(vc\right)_{z=\eta} - D\frac{\partial^2 \breve{c}}{\partial x^2} - \frac{1}{\eta}\left[D\frac{\partial c}{\partial z}\bigg|_{z=\eta} - D\frac{\partial c}{\partial z}\bigg|_{z=0}\right] = 0, \tag{A 1}$$

where overhead check marks indicate vertically averaged quantities: *e.g.* $\breve{c} = \eta^{-1}\int_0^\eta c\,dz$. We simplify the equation with the following assumptions: the vertical mass flux from the upper part of the layer to the lower part is negligible; the horizontal velocity in the upper part of the layer, u_{mz}, is vertically uniform and independent of x; and diffusion is negligible compared to advection outside of the boundary layer at $z = 0$. The averaged equation (A 1) becomes:

$$\frac{\partial \breve{c}}{\partial t} + u_{\mathrm{mz}}\frac{\partial \breve{c}}{\partial x} = \frac{1}{\eta}\left(-D\frac{\partial c}{\partial z}\right)_{z=0}. \tag{A 2}$$

The term on the right in parenthesis represents the diffusive flux into the upper part of the layer from the CO_2 source. We approximate this flux with the expression for the flux during convective shutdown (eq 3.5):

$$\left(-D\frac{\partial c}{\partial z}\right)_{z=0} = c_s V \kappa \left(1 - \breve{c}'\right)^2, \tag{A 3}$$

where we have equated $\overline{\overline{c'}}$ in equation 3.5 with $\breve{c}'$. Substituting this expression into equation A 2 and non-dimensionalizing the concentration using the saturated concentration yields:

$$\frac{\partial \breve{c}'}{\partial t} + u_{\mathrm{mz}}\frac{\partial \breve{c}'}{\partial x} = \frac{V\kappa}{\eta}\left(1 - \breve{c}'\right)^2. \tag{A 4}$$

This work was funded by the US Department of Energy (grants DE-SC0003907 and DE-FE0002041) and the MIT/Masdar Institute Program. Additional funding was provided by a Martin Fellowship for Sustainability (to MLS).

REFERENCES

Ascher, U. M., Ruuth, S. J. & Spiteri, R. J. 1997 Implicit-explicit Runge-Kutta methods for time-dependent partial differential equations. *Appl. Numer. Math.* **25**, 151–167.

Backhaus, S., Turitsyn, K. & Ecke, R. E. 2011 Convective instability and mass transport of diffusion layers in a Hele-Shaw geometry. *Phys. Rev. Lett.* **106**, 104501.

Bear, J. 1972 *Dynamics of Fluids in Porous Media*. Elsevier, New York, reprinted with corrections, Dover, New York, 1988.

Benson, S. M. & Cole, D. R. 2008 CO_2 sequestration in deep sedimentary formations. *Elements* **4** (5), 325–331.

Cheng, P. & Chang, I. 1976 Buoyancy induced flows in a saturated porous medium adjacent to impermeable horizontal surfaces. *Int. J. Heat Mass Trans.* **19**, 1267–1272.

Chiaramonte, L., Zoback, M. D., Friedmann, J. & Stamp, V. 2008 Seal integrity and feasibility of CO_2 sequestration in the Teapot Dome EOR pilot: geomechanical site characterization. *Environ. Geol.* **54** (8), 1667–1675.

Crank, J. 1980 *The Mathematics of Diffusion*. Oxford University Press.

De Josselin De Jong, G. 1981 The simultaneous flow of fresh and salt water in aquifers of large horizontal extension determined by shear flow and vortex theory. *Proc. Euromech.* **143**, 75–82.

Elder, J. W. 1967 Transient convection in a porous medium. *J. Fluid Mech.* **27** (3), 609–623.

Ennis-King, J., Preston, I. & Paterson, L. 2005 Onset of convection in anisotropic porous media subject to a rapid change in boundary conditions. *Phys. Fluids* **17**, 084107.

Grasso, J. R. 1992 Mechanics of seismic instabilities induced by the recovery of hydrocarbons. *Pure Appl. Geophys.* **139** (3/4), 507–534.

Gunter, W. D., Bachu, S. & Benson, S. 2004 The role of hydrogeological and geochemical trapping in sedimentary basins for secure geological storage of carbon dioxide. In *Geological Storage of Carbon Dioxide* (ed. S. J. Baines & R. H. Worden), *Geological Society, London, Special Publications*, vol. 233, pp. 129–145.

Hassanzadeh, H., Pooladi-Darvish, M. & Keith, D. W. 2007 Scaling behavior of convective mixing, with application to geological storage of CO_2. *AIChE J.* **53** (5), 1121–1131.

Hesse, M. A. 2008 Mathematical modeling and multiscale simulation for CO_2 storage in saline aquifers. PhD Thesis, Stanford University, Dept. of Energy Resources Engineering.

Hewitt, D. R., Neufeld, J. A. & Lister, J. R. 2013 Convective shutdown in a porous medium at high Rayleigh number. *J. Fluid Mech.* **719**.

Hidalgo, J. J., Fe, J., Cueto-Felgueroso, L. & Juanes, R. 2012 Scaling of convective mixing in porous media. *Phys. Rev. Lett.* **109**, 264503.

Huppert, H. E. & Woods, A. W. 1995 Gravity-driven flows in porous layers. *J. Fluid Mech.* **292**, 55–69.

751 IPCC 2005 *Special Report on Carbon Dioxide Capture and Storage, B. Metz et al. (eds.)*. Cam-
752 bridge University Press.
753 Kneafsey, T. J. & Pruess, K. 2010 Laboratory flow experiments for visualizing carbon
754 dioxide-induced, density-driven brine convection. *Transp. Porous Med.* **82**, 123–139.
755 Lackner, K. S. 2003 A guide to CO_2 sequestration. *Science* **300** (5626), 1677–1678.
756 Lambert, J. D. 1991 *Numerical Methods for Ordinary Differential Systems: The Initial Value*
757 *Problem*. Wiley.
758 LeVeque, R. J. 2002 *Finite Volume Methods for Hyperbolic Problems*. Cambridge University
759 Press.
760 MacMinn, C. W. & Juanes, R. 2013 Buoyant currents arrested by convective dissolution.
761 *Geophys. Res. Lett.* **40**, doi:10.1002/grl.50473.
762 Mathias, S. A., Hardisty, P. E., Trudell, M. R. & Zimmerman, R. W. 2009 Screening
763 and selection of sites for CO_2 sequestration based on pressure buildup. *Int. J. Greenh. Gas*
764 *Con.* **3**, 577–585.
765 Michael, K., Golab, A., Shulakova, V., Ennis-King, J., Allinson, G., Sharma, S. &
766 Aiken, T. 2010 Geological storage of CO_2 in saline aquifers—a review of the experience
767 from existing storage operations. *Int. J. Greenh. Gas Con.* **4**, 659–667.
768 Mito, S., Xue, Z. & Sato, T. 2013 Effect of formation water composition on predicting CO_2
769 behavior: a case study at the Nagaoka post-injection monitoring site. *Appl. Geochem.* **30**,
770 33–40.
771 Neufeld, J. A., Hesse, M. A., Riaz, A., Hallworth, M. A., Tchelepi, H. A. & Huppert,
772 H. E. 2010 Convective dissolution of carbon dioxide in saline aquifers. *Geophys. Res. Lett.*
773 **37**, L22404.
774 Nield, D. A. & Bejan, A. 2013 *Convection in Porous Media*, 4th edn. Springer.
775 Orr, Jr., F. M. 2009 Onshore geologic storage of CO_2. *Science* **325**, 1656–1658.
776 Pau, G. S. H., Bell, J. B., Pruess, K., Almgren, A. S., Lijewskia, M. J. & Zhang, K.
777 2010 High-resolution simulation and characterization of density-driven flow in CO_2 storage
778 in saline aquifers. *Adv. Water Resour.* **33** (4), 443–455.
779 Rapaka, S., Chen, S., Pawar, R., Stauffer, P. & Zhang, D. 2008 Non-modal growth of
780 perturbations in density-driven convection in porous media. *J. Fluid Mech.* **609**, 285–303.
781 Riaz, A., Hesse, M., Tchelepi, H. A. & Orr, Jr., F. M. 2006 Onset of convection in a
782 gravitationally unstable, diffusive boundary layer in porous media. *J. Fluid Mech.* **548**,
783 87–111.
784 Rutqvist, J. & Tsang, C. 2002 A study of caprock hydromechanical changes associated with
785 CO_2-injection into a brine formation. *Environ. Geol.* **42**, 296–305.
786 Schrag, D. P. 2007 Preparing to capture carbon. *Science* **315**, 812–813.
787 Slim, A. C., Bandi, M. M., Miller, J. C. & Mahadevan, L. 2013 Dissolution-driven con-
788 vection in a Hele-Shaw cell. *Phys. Fluids* **25**, 024101.
789 Slim, A. C. & Ramakrishnan, T. S. 2010 Onset and cessation of time-dependent, dissolution-
790 driven convection in porous media. *Phys. Fluids* **22**, 124103.
791 Strang, G. 2007 *Computational Science and Engineering*. Wellesley-Cambridge Press.
792 Szulczewski, M. L. & Juanes, R. 2013 The evolution of miscible gravity currents in horizontal
793 porous layers. *J. Fluid Mech.* **719**, 82–96.
794 Szulczewski, M. L., MacMinn, C. W., Herzog, H. J. & Juanes, R. 2012 Lifetime of carbon
795 capture and storage as a climate-change mitigation technology. *Proc. Natl. Acad. Sci. USA*
796 **109** (14), 5185–5189.
797 Underschultz, J., Boreham, C., Dance, T., Stalker, L., Freifeld, B., Kirste, D. &
798 Ennis-King, J. 2011 CO_2 storage in a depleted gas field: an overview of the CO2CRC
799 Otway Project and initial results. *Int. J. Greenh. Gas Con.* **5**, 922–932.
800 US Energy Information Administration, US Department of Energy 2009 Emis-
801 sions of greenhouse gases in the United States 2008. Report No. DOE/EIA-0573(2008),
802 http://www.eia.gov/oiaf/1605/ggrpt/pdf/0573(2008).pdf.
803 Wooding, R. A., Tyler, S. W. & White, I. 1997*a* Convection in groundwater below an
804 evaporating salt lake. 1. Onset of instability. *Water Resour. Res.* **33** (6), 1199–1217.
805 Wooding, R. A., Tyler, S. W. & White, I. 1997*b* Convection in groundwater below an
806 evaporating salt lake. 2. Evolution of fingers or plumes. *Water Resour. Res.* **33** (6), 1219–
807 1228.

808 Xu, X., Chen, S. & Zhang, D. 2006 Convective stability analysis of the long-term storage of
809 carbon dioxide in deep saline aquifers. *Adv. Water Resour.* **29**, 397–407.